

AFRL-SN-RS-TR-2005-410
Final Technical Report
January 2006



ALONG TRACK INTERFEROMETRY SYNTHETIC APERTURE RADAR (ATI-SAR) TECHNIQUES FOR GROUND MOVING TARGET DETECTION

Stiefvater Consultants

APPROVED FOR PUBLIC RELEASE; DISTRIBUTION UNLIMITED.

**AIR FORCE RESEARCH LABORATORY
SENSORS DIRECTORATE
ROME RESEARCH SITE
ROME, NEW YORK**

STINFO FINAL REPORT

This report has been reviewed by the Air Force Research Laboratory, Information Directorate, Public Affairs Office (IFOIPA) and is releasable to the National Technical Information Service (NTIS). At NTIS it will be releasable to the general public, including foreign nations.

AFRL-SN-RS-TR-2005-410 has been reviewed and is approved for publication

APPROVED: /s/

BRAHAM HIMED
Project Engineer

FOR THE DIRECTOR: /s/

RICHARD G. SHAUGHNESSY, Chief
Rome Operations Office
Sensors Directorate

REPORT DOCUMENTATION PAGE

Form Approved
OMB No. 074-0188

Public reporting burden for this collection of information is estimated to average 1 hour per response, including the time for reviewing instructions, searching existing data sources, gathering and maintaining the data needed, and completing and reviewing this collection of information. Send comments regarding this burden estimate or any other aspect of this collection of information, including suggestions for reducing this burden to Washington Headquarters Services, Directorate for Information Operations and Reports, 1215 Jefferson Davis Highway, Suite 1204, Arlington, VA 22202-4302, and to the Office of Management and Budget, Paperwork Reduction Project (0704-0188), Washington, DC 20503

1. AGENCY USE ONLY (Leave blank)		2. REPORT DATE JANUARY 2006	3. REPORT TYPE AND DATES COVERED Final Jul 03 – Jun 05	
4. TITLE AND SUBTITLE ALONG TRACK INTERFEROMETRY SYNTHETIC APERTURE RADAR (ATI-SAR) TECHNIQUES FOR GROUND MOVING TARGET DETECTION			5. FUNDING NUMBERS C - F30602-03-C-0212 PE - NA PR - JPLC TA - 15 WU - P1	
6. AUTHOR(S) Yuhong Zhang				
7. PERFORMING ORGANIZATION NAME(S) AND ADDRESS(ES) Stiefvater Consultants 10002 Hillside Terrace Marcy New York 13403			8. PERFORMING ORGANIZATION REPORT NUMBER N/A	
9. SPONSORING / MONITORING AGENCY NAME(S) AND ADDRESS(ES) Air Force Research Laboratory/SNRT 25 Electronic Parkway Rome New York 13441-4515			10. SPONSORING / MONITORING AGENCY REPORT NUMBER AFRL-SN-RS-TR-2005-410	
11. SUPPLEMENTARY NOTES AFRL Project Engineer: Braham Himed/SNRT/(315) 330-2552/ Braham.Himed@rl.af.mil				
12a. DISTRIBUTION / AVAILABILITY STATEMENT APPROVED FOR PUBLIC RELEASE; DISTRIBUTION UNLIMITED.				12b. DISTRIBUTION CODE
13. ABSTRACT (Maximum 200 Words) Conventional along track interferometric synthetic aperture radar, ATI-SAR, approaches can detect targets with very low radial speeds, but their false alarm rate is too high to be used in ground moving target indication radars. The report proposed a dual-threshold approach that combines the conventional interferometric phase detection and the SAR image amplitude detection in order to reduce the false alarm rate. The concept and performance of the dual-threshold approach were illustrated using the Jet Propulsion Laboratory AirSAR ATI data. A simple two-dimensional blind-calibration procedure was proposed to correct the group phase shift induced by the platform's crab angle. MATLAB programs for demonstrating the proposed approach were included.				
14. SUBJECT TERMS Space-Based Radar, Radar Signal Processing, Along-Track Interferometry (ATI), Synthetic Aperture Radar (SAR), Moving Target Detection, GMTI, Crab Angle Calibration, STAP, Experimental Data			15. NUMBER OF PAGES 62	
			16. PRICE CODE	
17. SECURITY CLASSIFICATION OF REPORT UNCLASSIFIED	18. SECURITY CLASSIFICATION OF THIS PAGE UNCLASSIFIED	19. SECURITY CLASSIFICATION OF ABSTRACT UNCLASSIFIED	20. LIMITATION OF ABSTRACT UL	

Table of Contents

1.0	Introduction	1
1.1	Background	1
1.2	Space-Time Adaptive Processing	2
1.3	ATI-SAR Approach	5
2.0	Basic Measurement Principles	7
2.1	“Ping-Pong” Mode	9
2.2	Standard Mode	10
2.3	Double Baseline Mode	11
2.4	Summary and Examples	12
2.4.1	<i>L-Band Example</i>	12
2.4.2	<i>C-Band Example</i>	13
3.0	Detection Performance of Conventional ATI-SAR	15
3.1	False Alarm Rate	15
3.1.1	<i>Probability Density Function of Interferometric Phase</i>	15
3.1.2	<i>Numerical Examples</i>	16
3.2	Probability of Detection	20
4.0	New C-Band AirSAR ATI Data	22
4.1	Data and System Parameters	22
4.1.1	<i>“Ping-Pong” Mode</i>	24
4.1.2	<i>Standard and Double Baseline Modes</i>	24
4.2	Stripmap SAR Images	25
4.2.1	<i>Cross-Range Resolution</i>	25
4.2.2	<i>SAR Images</i>	26
5.0	Blind Calibration for Group Phase Shift Induced by Crab Angle	34
5.1	Group Phase Shift Induced by Crab Angle	34
5.2	Two-Dimensional Blind Calibration for Interferometric Phase	37

5.3	In Illustration Example	38
6.0	Moving Target Detection Using ATI-SAR.....	42
6.1	Phase-Only Detection	42
6.2	Amplitude-Only Detection.....	42
6.3	Dual-Threshold Detection.....	43
6.4	Applying the Dual-Threshold Approach to Other ATI-Mode Data	46
6.4.1	“Standard” Mode Data.....	46
6.4.2	“Double Baseline” Mode	49
7.0	Conclusions	53
8.0	Reference.....	54

List of Figures

Figure 1. Space-based radar concept: satellite coverage provides wide-area surveillance and tracking of airborne and ground moving targets.	2
Figure 2. SINR performance for MF and JDL.	4
Figure 3. Three ATI data collection modes.	8
Figure 4. Principles of ATI-SAR (“ping-pong” mode).	9
Figure 5. Equivalent single antenna SAR for a two-antenna stripmap-SAR.	10
Figure 6. Interferometric phase as a function of target velocities (L-Band).	13
Figure 7. Interferometric phase as a function of target velocities (C-Band).	14
Figure 8. Phase noise <i>pdf</i> for different CNR values with $\gamma_c = 0.98$	17
Figure 9. False alarm rate for different CNR values with $\gamma_c = 0.98$	17
Figure 10. Phase noise <i>pdf</i> for different CNR values with $\gamma_c = 0.99$	18
Figure 11. False alarm rate for different CNR values with $\gamma_c = 0.99$	18
Figure 12. Phase noise <i>pdf</i> for different CNR values with $\gamma_c = 1$	19
Figure 13. False Alarm probability for different CNR values with $\gamma_c = 1$	19
Figure 14. Phase <i>pdf</i> for three different SCR values in presence of a moving target.	21
Figure 15. Detection probability for three different SCR values in presence of a moving target.	21
Figure 16. Map of Lancaster, CA.	22
Figure 17. AirSAR instrument (panels behind wing) mounted aboard a modified NASA DC-8 aircraft.	23
Figure 18. Stripmap SAR images using the C-band AirSAR data.Cont.)	27
Figure 19. Newly taken bird-eye picture in the area of Mojave Airport, CA.	33
Figure 20. Across-track offset between two antennas induced by the crab (yaw) angle.	35
Figure 21. Group phase shift induced by yaw angle as a function of slant range (“ping-pong” mode).	36
Figure 22. Group phase shift induced as a function of slant range (Yaw: 5°).	36
Figure 23. Image A for selected area (from Patch 3).	39
Figure 24. Interferometric phase map before the phase calibration for crab angle.	39
Figure 25. Histogram of interferometric phase before phase calibration.	40
Figure 26. Interferometric phase map after the phase calibration.	40
Figure 27. Histogram of interferometric phase after the phase calibration.	41
Figure 28. Interferometric phase map with $\eta_\theta = 1$ radian.	42
Figure 29. SAR amplitude image with $\eta_a = 6$ dB.	43
Figure 30. Interferometric phase map with $\eta_\theta = 1$ radian and $\eta_a = 6$ dB.	45
Figure 31. Amplitude map with $\eta_\theta = 1$ radian and $\eta_a = 6$ dB.	45
Figure 32. Positions of potential targets (red points) on the SAR image (“ping-pong”).	46
Figure 33. Interferometric phase map with $\eta_\theta = 1$ radian (“standard”).	47
Figure 34. SAR amplitude image with $\eta_a = 6$ dB (“standard”).	47
Figure 35. Interferometric phase map with $\eta_\theta = 1$ radian and $\eta_a = 6$ dB (“standard”)....	48

Figure 36. Amplitude map with $\eta_\theta = 1$ radian and $\eta_a = 6$ dB (“standard”).	48
Figure 37. Positions of potential targets (red points) on the SAR image (“standard”).	49
Figure 38. Interferometric phase map with $\eta_\theta = 1$ radian (“double baseline”).	50
Figure 39. Amplitude image with $\eta_a = 6$ dB (“double baseline”).	50
Figure 40. Interferometric phase map with $\eta_\theta = 1$ radian and $\eta_a = 6$ dB (“double baseline”).	51
Figure 41. SAR Amplitude map with $\eta_\theta = 1$ radian and $\eta_a = 6$ dB (“double baseline”).	51
Figure 42. Positions of potential targets (red points) on the SAR image (“double baseline”).	52

List of Tables

Table 1. System and scenario parameters.	3
Table 2. Summary of equations for three ATI-SAR modes.	12
Table 3. MDV and unambiguous velocities for three ATI-SAR modes (L-Band).	13
Table 4. MDV and unambiguous velocities for three ATI-SAR modes (C-Band).	14
Table 5. P_{FA} vs. CNR and phase threshold ($\gamma_c = 0.98$).	20
Table 6. P_{FA} vs. CNR and phase threshold ($\gamma_c = 0.99$).	20
Table 7. P_{FA} vs. CNR and phase threshold ($\gamma_c = 1$).	20
Table 8. Information of received C-band AirSAR ATI data.	22
Table 9. Cross-range resolution (ΔR_c) in meters.	26

1.0 Introduction

This document is the final technical report for the project titled "Development of Signal Processing Algorithms for Space-Based Radars", under Contract BAA-00-07-IFKPA, which was performed by Stiefvater Consultants for the Air Force Research Laboratory, Sensors Directorate (SNRT), located in Rome, New York. The objective of this effort was to develop signal-processing algorithms for the detection of ground moving targets using space-based radars (SBR). Particularly, this report summarizes our work on the along-track interferometric synthetic aperture radar (ATI-SAR) approach for detecting moving targets.

1.1 Background

Historically, Ground Moving Target Indication (GMTI) has been accomplished using manned airborne platforms, such as the Joint Surveillance Target Attack Radar System (Joint STARS). Recently, there has been a growing interest in augmenting these airborne assets with a space-based capability. Such a system would be capable of providing both wide-area (theatre) surveillance and tracking of airborne and ground moving targets. The space-based radar (SBR) capability (Figure 1) is particularly attractive because it provides: (1) deep coverage into areas typically denied airborne assets; (2) greater ease and flexibility for deploying the sensor platform on station and meeting coverage tasking; (3) greater area coverage rate performance; and (4) a steep lookdown capability for foliage penetration (FOPEN) operation.

Space-based surveillance requires a nominal area coverage rate of several hundred km^2/s with revisit rates of one to two minutes, while tracking requires somewhat shorter revisit times. Thus, a constellation of satellites would be necessary to meet these requirements.

Even though it may seem that the altitude of a satellite can be freely chosen, the two Van Allen radiation belts limit practical orbit selection. The two Van Allen radiation belts are centered on the earth's geo-magnetic axis, at altitudes ranging from 1500km to 5000km and from 13,000 to 20,000 km. To minimize the radiation damage to electronic components in a lightweight, unshielded satellite design, the satellites would have to be placed in orbits

outside of these belts. Therefore, either a medium-earth orbit (MEO) at altitudes of 5000km to 13000km or a low-earth orbit (LEO) at an altitude less than 1500km is desirable.

Today, both LEO and medium-earth orbit MEO constellations are being considered for SBR. Ultimately, the orbit selection will depend on the exact system requirements and the total life-cycle cost. Although smaller numbers of satellites would be required at MEO altitudes than at LEO altitudes to meet the large surveillance coverage requirements, the low life-cycle costs (including payload plus launcher) make LEO satellites more attractive for regional coverage than their MEO counterparts. This effort focuses on a LEO constellation. The high orbital velocity and large clutter range span make clutter suppression and detection of slow-moving targets more difficult.

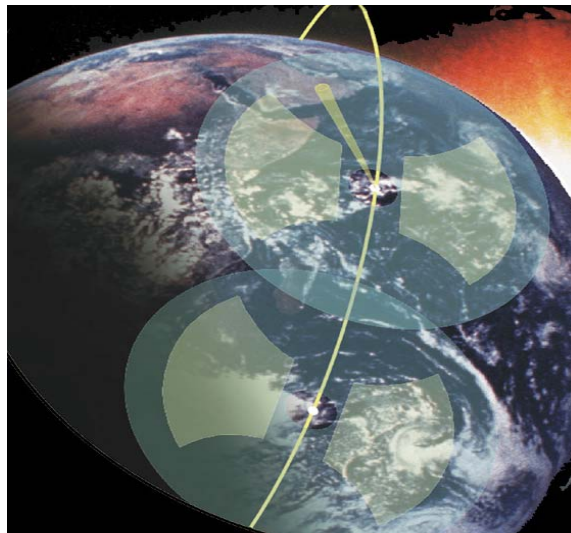


Figure 1. Space-based radar concept: satellite coverage provides wide-area surveillance and tracking of airborne and ground moving targets.

1.2 Space-Time Adaptive Processing

The ability of an SBR system to suppress the clutter interference is complicated by the large platform velocities associated with SBR operation. Such operation generally requires the detection of targets within the clutter Doppler spectrum (endo-clutter case). The

challenge is more pronounced at LEO deployments where orbit speeds are much larger. For example, the mainbeam clutter velocity spectrum for a LEO satellite with a speed of 7,612 m/s (at an altitude of 500 km), and a 50-meter antenna in azimuth operating at L-band, is about ± 36.5 m/sec. In other words, all targets with speed between -36.5 to $+36.5$ m/sec are immersed in main beam ground clutter, making target detection using conventional pulse-Doppler (PD) processing questionable.

Three decades of research and development has shown that space-time adaptive processing (STAP) [1] is a potentially attractive technique for clutter suppression in airborne radars. It could be effective in SBR applications as well [2]. However, space-based STAP is a much more difficult problem than its airborne counterpart and may not meet the requirement on Minimal Detectable Velocity (MDV), because of the high platform speed and large clutter extension. To illustrate this, consider an L-band radar with a 50 m x 2 m phased array carried by a low-earth orbit (LEO) satellite at a 500 km altitude. Using the high-fidelity Signal Modeling and Simulation (SMS) tool [3], we simulated the clutter covariance matrix with the assumed system and scenario parameters listed in Table 1.

Table 1. System and scenario parameters.

Parameter	Value	Comments
Antenna Size	50 m x 2 m	
Number of Panels	32	No overlap
Panel Size	12 by 12 elements	
Center Frequency	1260 MHz	
Bandwidth	10 MHz	
PRF	2000 Hz	
Duty Cycle	8 %	
Pulse Number	16	Each CPI
Xmt Weighting	Uniform	
Rcv Weighting	Uniform	Uniform within subarray
Platform Height	500 km	Inertial speed: 7612.61 m/s
Orbit Type	Polar, circular	
Elevation Scan Angle	-28.3°	Mechanically
Slant Range of Interest	1258.15 km	Grazing angle: 18.322°

Figure 2 shows the SINR loss (i.e. loss relative to the clutter-free case) as a function of Doppler frequency for the Matched Filter (MF) [1] and the joint-domain localized (JDL) algorithm [4]. The JDL algorithm is a post-Doppler beam-domain approach. It first transforms the radar data cube into the beam-Doppler domain, and then performs a joint-domain adaptation over a $N_0 \times J_0$ local processing region (LPR), where N_0 is the number of Doppler bins and J_0 is the number of spatial beams. The low degrees-of-freedom (DOF) requirement characterized by this algorithms leads to a significant reduction in required sample support and computational load. Figure 2 shows an example with a 3x3 (3 Doppler bins and 3 spatial beams) LPR. The corresponding MDV, measured assuming a -5 dB SINR loss threshold, is 13.81 m/s for MF and 18.62 m/s for JDL. For a space-based GMTI radar, the requirement on MDV could be under 1m/s. Obviously, a STAP-based approach cannot meet the MDV requirement for this example LEO system. Even worse, earth's rotation will induce a crab angle to the platform, which makes the clutter range-Doppler spectrum vary with range [5] and further degrades the SINR and MDV performance of STAP [6].

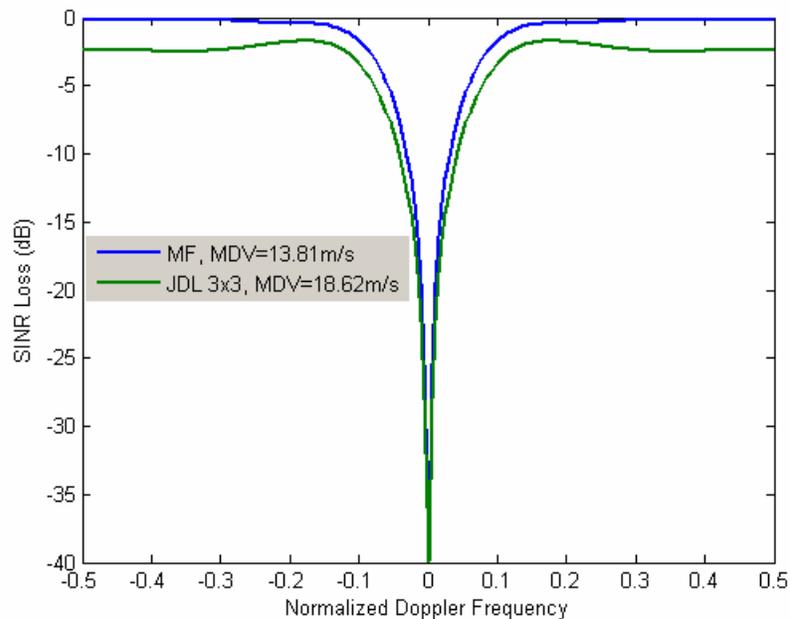


Figure 2. SINR performance for MF and JDL.

1.3 ATI-SAR Approach

For targets moving at speeds slower than the endo-clutter velocity, alternative GMTI techniques may be needed to supplement conventional STAP processing. One such technique is the Along Track Interferometric Synthetic Aperture Radar (ATI-SAR^{*}) [7]. The ATI-SAR technique is based on the acquisition of two complex SAR images taken under identical geometries separated by a short time interval. The phase difference between the two interferometric images is used as a test statistic to be compared with a decision threshold. The ATI-SAR technique has been proven valuable to sense the earth-surface motion such as ocean surface currents, where the speed accuracies in the order of a few centimeters per second were reported from airborne platforms [7]. Recently, there has been increasing interest in applying ATI-SAR techniques for the detection of slow moving targets, especially GMTI, using space-based assets [8]. A major objective of this effort is to assess and develop the ATI-SAR techniques for detecting slow moving ground targets.

First, the detection performance of conventional ATI-SAR is examined. It is shown that the high false alarm rate associated with this technique would be a big concern for any military application. To reduce the false alarm rate, a dual-threshold approach that combines the conventional interferometric phase detection with the SAR image amplitude detection is proposed in this work. Pixels with strong returns could contain moving targets, stationary objects, and other discretely. The amplitude detection suppresses the weak returns from large smooth surfaces such as road and water surfaces. This yields two important results:

(1) An interferometric phase map (including target velocity information) obtained by applying the interferometric phase detection only to the pixels selected by the amplitude detection,

* Also known as AT InSAR, IFSAR etc.

(2) An amplitude map (including target strength information) obtained by applying the amplitude detection only to the pixels selected by the interferometric phase detection.

We have illustrated this concept [9] using the Jet Propulsion Laboratory (JPL) L-band AirSAR ATI data, collected in November 1998, in the Monterey Bay area, CA. Further results using JPL's new C-band AirSAR ATI data collected in April 2004, in the area of Lancaster, CA, are presented in this report.

The ATI-SAR processing also requires a precise calibration of the platform's crab angle. Because the data were collected from an airborne platform, the crab angle was varying during the data acquisition flight. Reference [10] developed a calibration method based on the inertial navigation unit (INU) measured attitude data and an array of known stationary corner reflectors (strong scatterers) as the reference. In this report, it is shown that the crab angle induces a range-dependent modulation to the interferometric phase and a blind calibration method that does not require any knowledge of the ground reference scatterer and/or the actual crab angle is introduced.

The new C-band AirSAR ATI data we received are collected in the following three modes[11], which will be explained in the next Section:

- Standard mode: Single baseline, single transmitter.
- "Ping-pong " mode: Zero baseline.
- Double baseline mode: Double baseline.

The AirSAR data include two 2.5 GB image data files and many supportive files for each mode.

2.0 Basic Measurement Principles

The ATI-SAR technique is based on the acquisition of two complex SAR images, taken under identical geometries separated by a short time interval, with the interferometric phase being used as a test statistic.

Throughout this section, we assume that the SAR data are collected in an ideal unsquinted (zero-Doppler) stripmap mode [12] through two antennas located along the track with separation B_x between their phase centers. We further assume that the platform moves along a straight and level trajectory at a height H_p and speed V_p . An approach for overcoming crab angle effects will be presented in Section 5.0.

Figure 3 shows three ATI data collection modes used in the JPL's AirSAR data. The "standard" mode uses a single transmitter where one antenna transmits and both antennas receive. The "ping-pong" mode uses dual transmitters where each antenna alternately transmits and receives its own echoes. The double baseline mode also uses dual transmitters, but one antenna receives echoes transmitted by another antenna and the two channels of data are alternately collected on adjacent pulses.

As an electromagnetic wave travels a round-trip distance 2ρ to and from a scatterer, the phase changes by

$$\varphi = -4\pi\rho/\lambda, \quad (1)$$

where λ is the wavelength of the radiation. The Doppler shift of a scatterer is

$$f_D = \frac{1}{2\pi} \frac{d\varphi}{dt} = -\frac{2\dot{\rho}}{\lambda} \quad (2)$$

where $\dot{\rho}$ is the range rate.

If Image B is taken at a short time interval Δt lagged to Image A under otherwise identical conditions, the interferometric phase for a scatterer can be expressed as

$$\theta = 2\pi f_D \Delta t = \frac{4\pi}{\lambda} \Delta t V_t \quad (3)$$

where $V_t = -\dot{\rho}$ is the radial speed of the scatterer.

With a threshold η_0 , which is determined by the required false alarm rate, the test statistic can be expressed as

$$\begin{cases} |\theta| \geq \eta_0, & H_0 \\ |\theta| < \eta_0, & H_1 \end{cases} \quad (4)$$

And the MDV can be expressed as

$$\text{MDV} = \frac{\lambda \eta_0}{4\pi \Delta t} \quad (5)$$

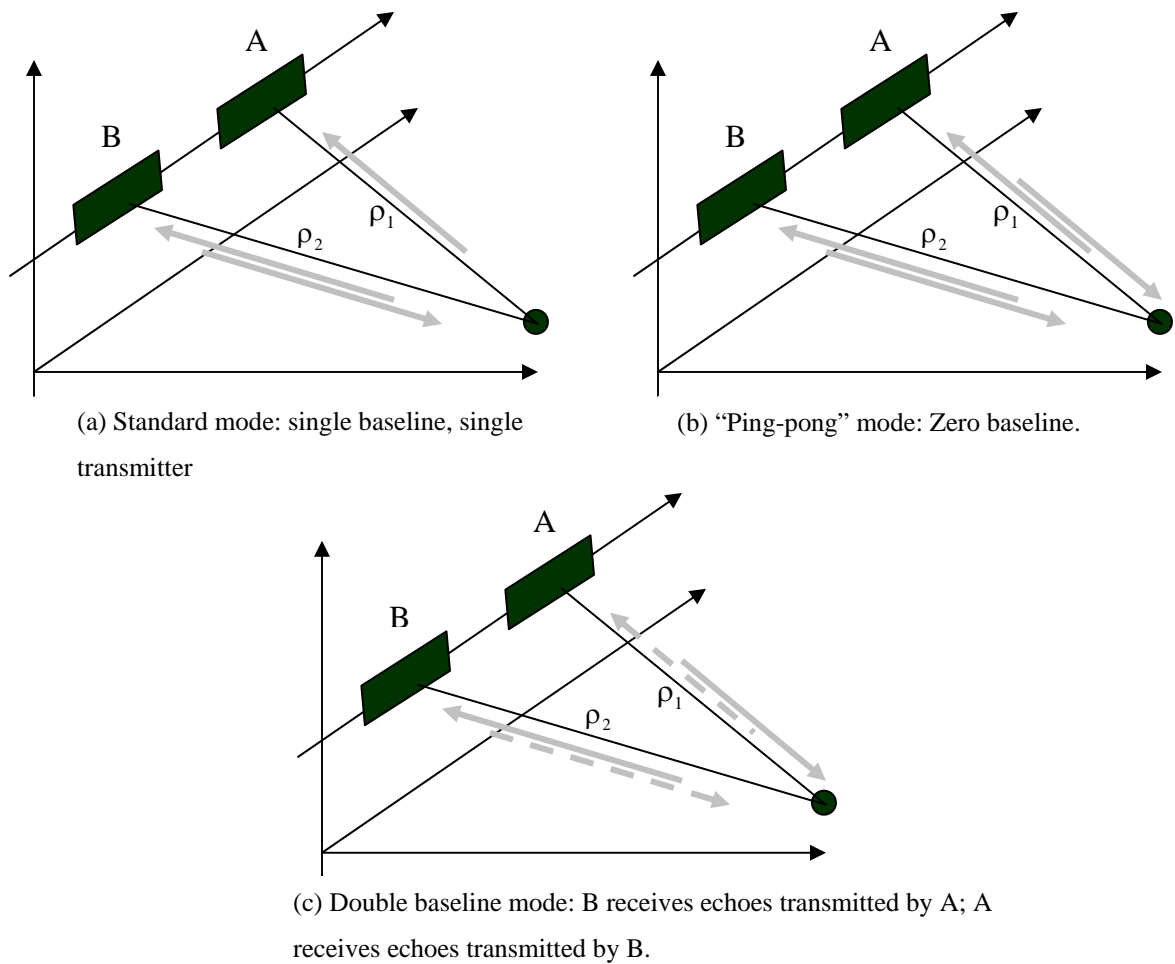


Figure 3. Three ATI data collection modes.

2.1 “Ping-Pong” Mode

In the “ping-pong” mode, Images A and B are acquired from the fore-antenna and the aft-antenna, respectively, as shown in Figure 4, The time delay is defined as the time required for the aft-antenna’s traveling to the fore-antenna position, which is calculated as

$$\Delta t = B_x / V_p, \quad (6)$$

where B_x is the baseline distance between the phase centers of two antennas, and V_p is the platform velocity. The interferometric phase can be rewritten as

$$\theta = \frac{4\pi B_x}{\lambda V_p} V_t. \quad (7)$$

The maximum unambiguous ATI velocity can be found, by letting $\theta = 2\pi$, as

$$V_{\text{unamb}} = \frac{\lambda V_p}{2B_x}. \quad (8)$$

The ATI system can measure velocities unambiguously if $|V_t| < V_{\text{unamb}} / 2$, and the MDV becomes

$$\text{MDV} = \frac{\lambda V_p \eta_\theta}{4\pi B_x}. \quad (9)$$

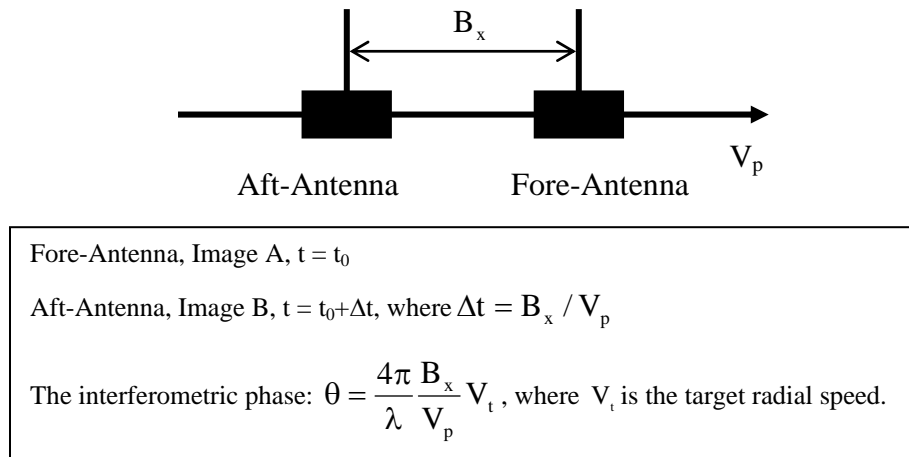


Figure 4. Principles of ATI-SAR (“ping-pong” mode).

2.2 Standard Mode

In this mode, Image B is the same as that obtained in the “ping-pong” mode, but Image A is formed using two separate antennas (one transmits, another receives).

In an ideal unsquinted stripmap mode [12], the SAR pixels are formed from zero-Doppler output. From the geometry in Figure 5, we can see that the stripmap SAR image using two antennas is equivalent to that obtained with a single antenna located in the middle between two antennas (generally at the cross point between the bisector line and the baseline).

Therefore, the standard mode interferometric SAR is equivalent to a “ping-pong” mode with half the baseline distance, i.e. $B_x/2$. Thus, the interferometric phase can be rewritten as

$$\theta = \frac{2\pi}{\lambda} \frac{B_x}{V_p} V_t. \quad (10)$$

The maximum unambiguous ATI velocity becomes

$$V_{\text{unamb}} = \frac{\lambda V_p}{B_x}. \quad (11)$$

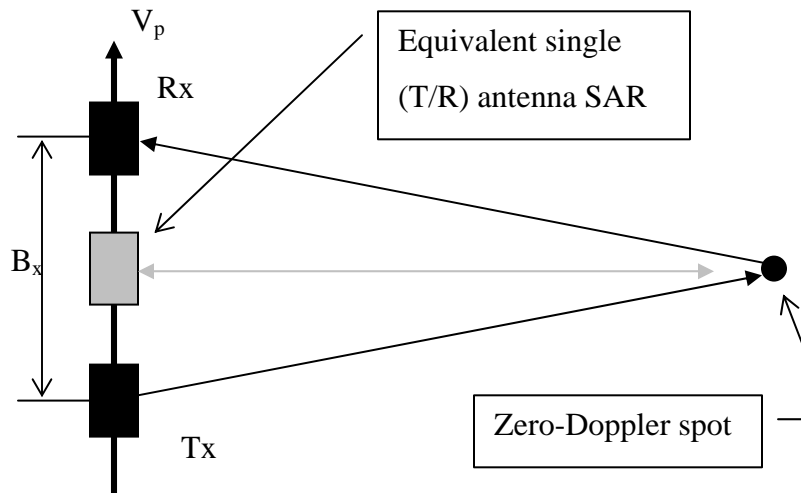


Figure 5. Equivalent single antenna SAR for a two-antenna stripmap-SAR.

The MDV becomes

$$\text{MDV} = \frac{\lambda V_p \eta_\theta}{2\pi B_x}. \quad (12)$$

2.3 Double Baseline Mode

The double baseline mode also uses dual transmitters, but one antenna receives echoes transmitted by another antenna and the two channels of data are alternately collected on adjacent pulses. The time difference between two images is one pulse repetition interval (PRI), i.e.,

$$\Delta t = T, \quad (13)$$

where $T = 1/\text{PRF}$ is PRI as PRF is the pulse repetition frequency. The interferometric phase can be rewritten as

$$\theta = \frac{4\pi}{\lambda} T V_t. \quad (14)$$

The maximum unambiguous ATI velocity can be found, by letting $\theta = 2\pi$, as

$$V_{\text{unamb}} = \frac{\lambda}{2T}. \quad (15)$$

The MDV becomes

$$\text{MDV} = \frac{\lambda \eta_\theta}{4\pi T}. \quad (16)$$

2.4 Summary and Examples

Table 2 lists the expressions derived above for three ATI-SAR modes. Two numerical examples associated with JPL's AirSAR system [10] are presented.

Table 2. Summary of equations for three ATI-SAR modes.

Mode	Ping-Pong	Standard	Double Baseline
Interferometric Phase θ	$\frac{4\pi B_x}{\lambda} \frac{V_t}{V_p}$	$\frac{2\pi B_x}{\lambda} V_t$	$\frac{4\pi}{\lambda} T V_t$
Unambiguous ATI Velocity V_{unamb} (m/s)	$\frac{\lambda V_p}{2B_x}$	$\frac{\lambda V_p}{B_x}$	$\frac{\lambda}{2T}$
MDV (m/s)	$\frac{\lambda V_p \eta_\theta}{4\pi B_x}$	$\frac{\lambda V_p \eta_\theta}{2\pi B_x}$	$\frac{\lambda \eta_\theta}{4\pi T}$

2.4.1 L-Band Example

A typical set of parameters associated with JPL's L-band AirSAR system are:

- $V_p = 216$ m/s,
- $\lambda = 0.2424$ m,
- $B_x = 19.7736$ m, and
- PRF = 420 Hz.

Figure 6 shows the interferometric phase as a function of target velocity for the three ATI modes discussed above. Table 3 shows the corresponding MDV and unambiguous velocities. It is shown that the 'ping-pong' mode provides the best MDV, but the lowest unambiguous velocity, and the "double baseline" mode provides the worst MDV, but the highest unambiguous velocity. It may be necessary to combine these modes and probably STAP-based approach to cover the GMTI velocity range of interest.

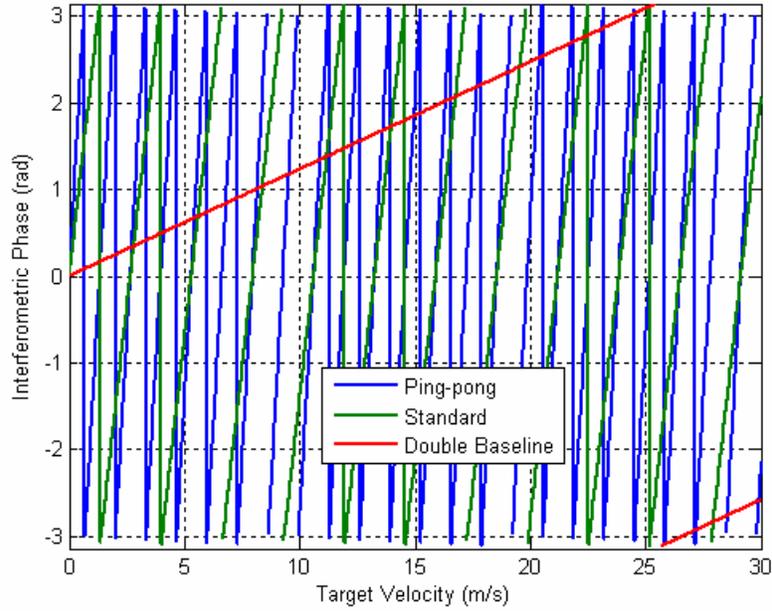


Figure 6. Interferometric phase as a function of target velocities (L-Band).

Table 3. MDV and unambiguous velocities for three ATI-SAR modes (L-Band).

Mode	Ping-Pong	Standard	Double Baseline
Unambiguous ATI Velocity V_{unamb} (m/s)	2.9281	5.8562	15.9894
MDV (m/s) for $\eta_0 = 1$ radian	0.2107	0.4214	8.1016
MDV (m/s) for $\eta_0 = 1.5$ radian	0.3161	0.6321	12.1524

2.4.2 C-Band Example

A typical set of parameters associated with JPL's C-band AIRSAR system are:

- $V_p = 214.77$ m/s,
- $\lambda = 5.67$ cm,
- $B_x = 2.0794$ m, and
- PRF = 564 Hz.

Figure 7 shows the interferometric phase as a function of target velocity for the three ATI modes discussed above. Table 4 shows the corresponding MDV and unambiguous velocities.

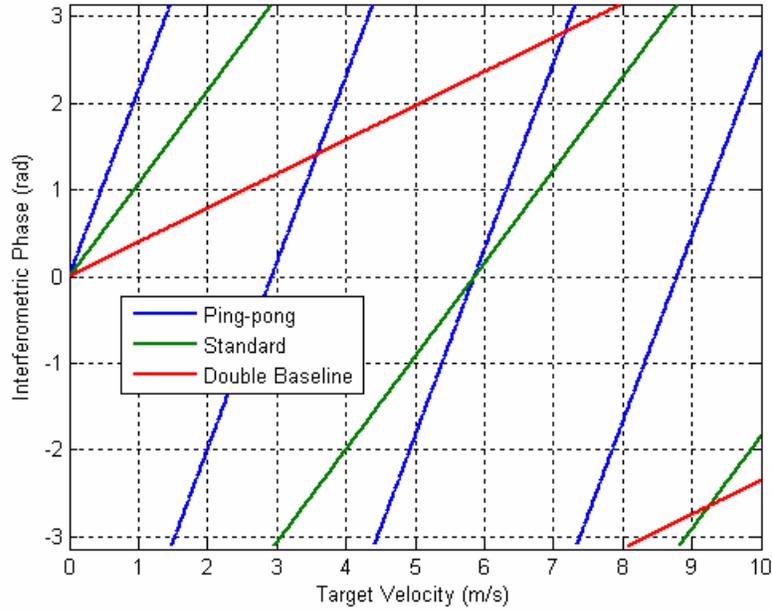


Figure 7. Interferometric phase as a function of target velocities (C-Band).

Table 4. MDV and unambiguous velocities for three ATI-SAR modes (C-Band).

Mode	Ping-Pong	Standard	Double Baseline
Unambiguous ATI Velocity V_{unamb} (m/s)	2.9281	5.8562	15.9894
MDV (m/s) for $\eta_0 = 1$ radian	0.4660	0.9320	2.5448
MDV (m/s) for $\eta_0 = 1.5$ radian	0.6990	1.3981	3.8172

3.0 Detection Performance of Conventional ATI-SAR

3.1 False Alarm Rate

The probability of false alarm (or false alarm rate), P_{FA} , can be calculated from the probability density function (*pdf*) of the interferometric phase in the absence of target. For simplicity, consider a Gaussian clutter associated with a homogeneous background and additive white Gaussian thermal noise. In the absence of target, the interferogram is the product of two complex Gaussian correlated signals.

3.1.1 Probability Density Function of Interferometric Phase

Assume that two corresponding pixels in Images A and B, x_1 and x_2 , are joint circular Gaussian variables with zero mean. The joint probability density function (*pdf*) is given by

$$pdf(\mathbf{w}) = \frac{1}{\pi^2 |\mathbf{C}|} \exp\{-\mathbf{w}^H \mathbf{C} \mathbf{w}\} \quad (17)$$

where

$$\mathbf{w} = \begin{bmatrix} x_1 \\ x_2 \end{bmatrix}, \quad (18)$$

The correlation matrix can be written as

$$\mathbf{C} = E\{\mathbf{w}\mathbf{w}^H\} = \begin{pmatrix} \bar{I}_1 & \gamma \bar{I} \\ \gamma^* \bar{I} & \bar{I}_2 \end{pmatrix} \quad (19)$$

where

$$\begin{aligned} \bar{I}_1 &= E[|x_1|^2], \\ \bar{I}_2 &= E[|x_2|^2], \text{ and} \\ \bar{I} &= \sqrt{\bar{I}_1 \bar{I}_2} \end{aligned} \quad (20)$$

and γ is the correlation coefficient.

The interferogram is a new random variable, given by

$$v = x_1 x_2^* \quad (21)$$

The joint *pdf* of the magnitude and phase of v can be found to be

$$\text{pdf}(|v|, \phi) = \frac{2|v|}{\pi \bar{I}^2(1-|\gamma|^2)} \exp\left\{ \frac{2|\gamma||v|\cos\phi}{\bar{I}(1-|\gamma|^2)} \right\} K_0\left(\frac{2|v|}{\bar{I}(1-|\gamma|^2)} \right), \quad (22)$$

where $K_0(\cdot)$ is the modified Bessel function of the second kind of order 0.

The marginal *pdf* of the interferometric phase is derived by Bamler and Hartl in [14]:

$$\text{pdf}(\phi) = \frac{1-|\gamma|^2}{2\pi} \frac{1}{1-|\gamma|^2 \cos^2 \phi} \left[1 + \frac{|\gamma|\cos\phi \cos^{-1}(-|\gamma|\cos\phi)}{\sqrt{1-|\gamma|^2 \cos^2 \phi}} \right], \quad (23)$$

which is fully characterized by the correlation coefficient $|\gamma|$.

In the presence of additive white noise, the above *pdf* formula for the interferometric phase holds true with the equivalent correlation coefficient

$$\gamma = \frac{\gamma_c}{1+1/\text{CNR}}, \quad (24)$$

where γ_c is the clutter correlation coefficient and CNR is the clutter-to-noise power ratio.

3.1.2 Numerical Examples

Figures 8, 10 and 12 show the *pdf* of the interferometric phase in the absence of target, for different CNR and $\gamma_c = 0.98, 0.99, \text{ and } 1$, respectively. The corresponding false alarm rates vs. the phase threshold η_0 are shown in Figures 9, 11, and 13, respectively. The numerical results are listed in Tables 5 through 7. For example, $P_{\text{FA}} = 5.4 \times 10^{-3}$ for $\gamma_c = 1$ and $\eta_0 = 1.5$ radians, which is a very high false alarm rate for any surveillance radar.

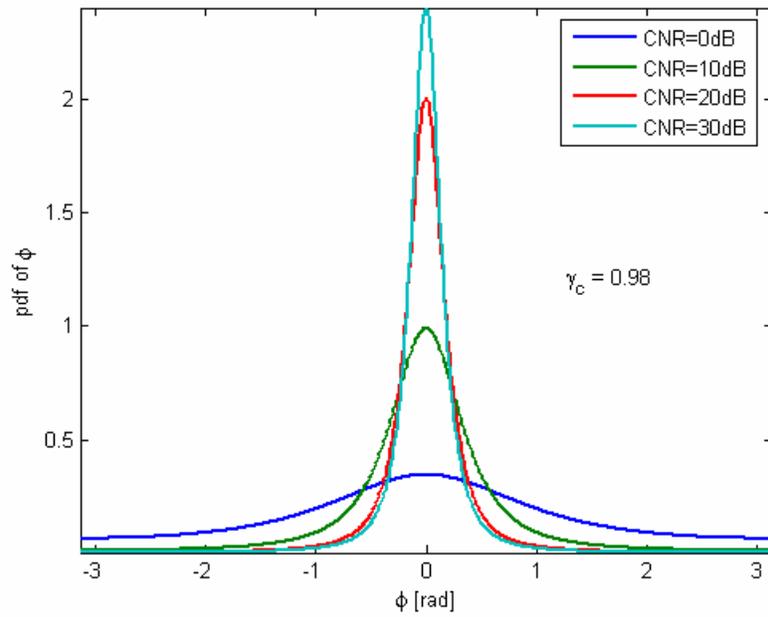


Figure 8. Phase noise *pdf* for different CNR values with $\gamma_c = 0.98$.

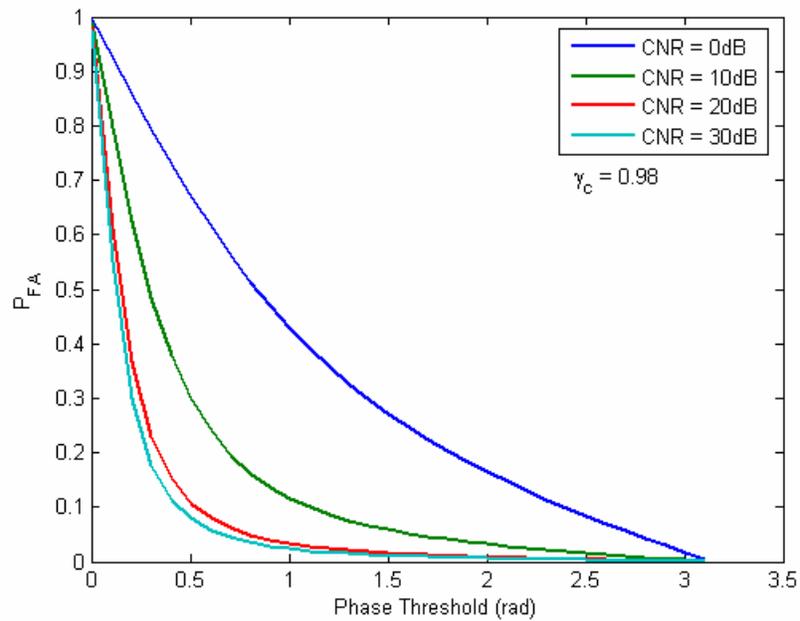


Figure 9. False alarm rate for different CNR values with $\gamma_c = 0.98$

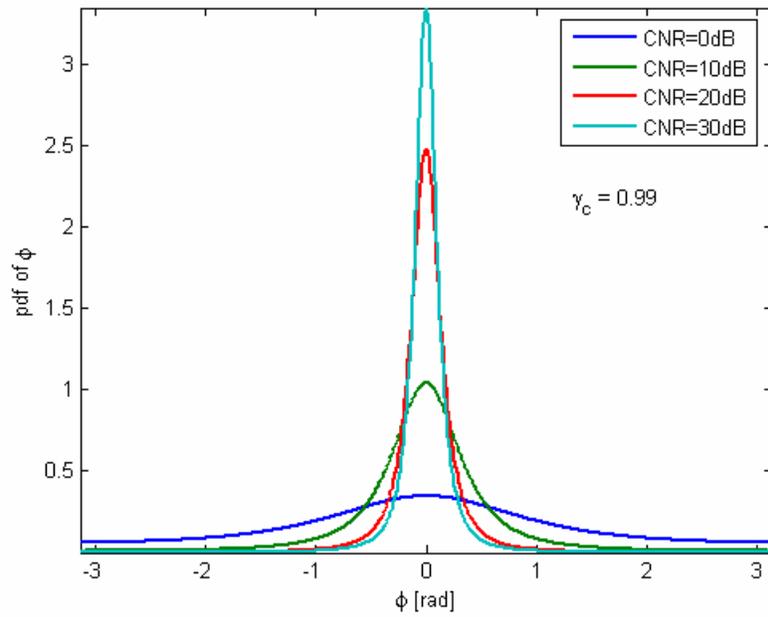


Figure 10. Phase noise *pdf* for different CNR values with $\gamma_c = 0.99$.

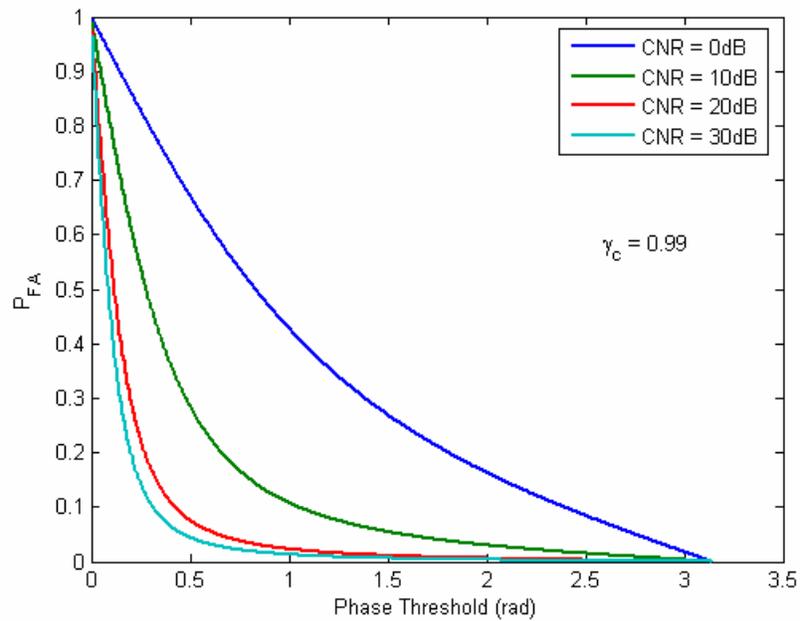


Figure 11. False alarm rate for different CNR values with $\gamma_c = 0.99$.

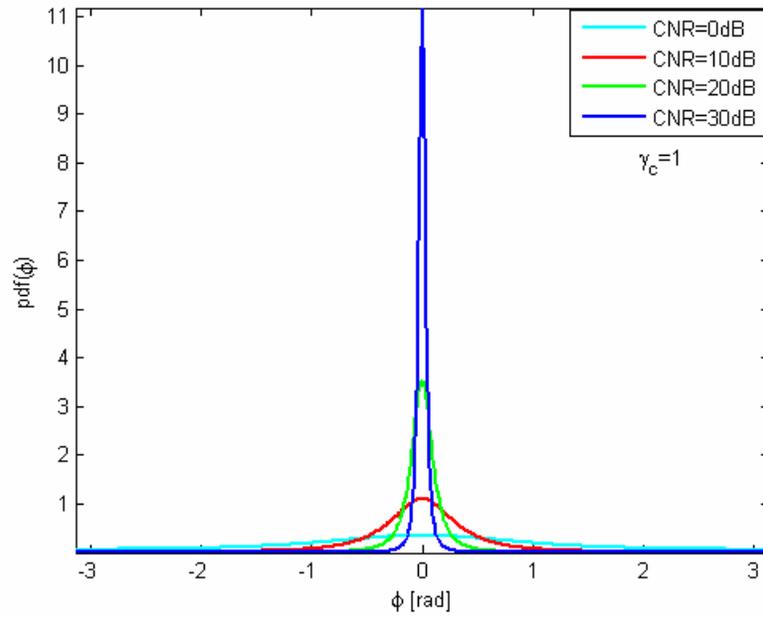


Figure 12. Phase noise *pdf* for different CNR values with $\gamma_c = 1$.

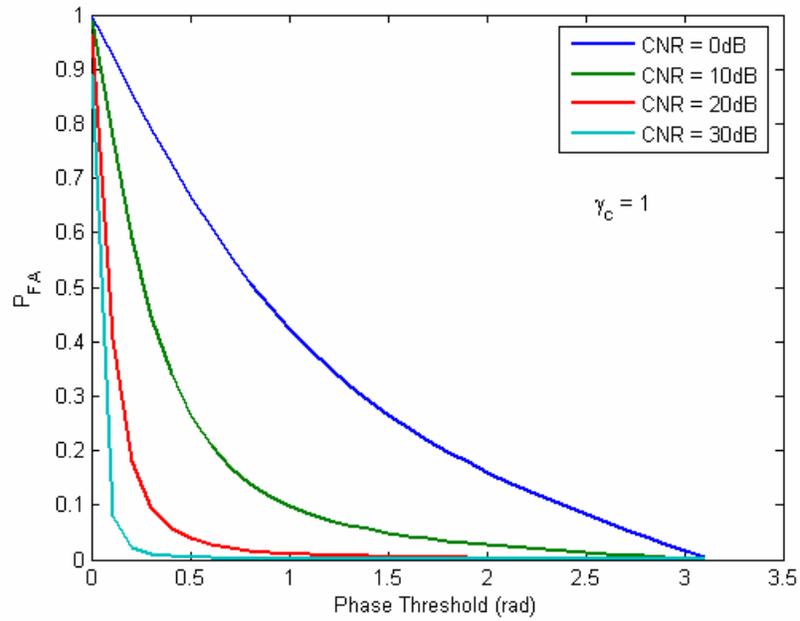


Figure 13. False Alarm probability for different CNR values with $\gamma_c = 1$

Table 5. P_{FA} vs. CNR and phase threshold ($\gamma_c = 0.98$).

CNR \ η_θ (rad.)	0.5	1	1.5	2	2.5
0 dB	0.6737	0.4312	0.2724	0.1654	0.0855
10 dB	0.3025	0.1173	0.0594	0.0327	0.0162
20 dB	0.1095	0.0339	0.0162	0.0088	0.0043
30 dB	0.0804	0.0241	0.0115	0.0062	0.0030
40 dB	0.0773	0.0231	0.0110	0.0059	0.0029

Table 6. P_{FA} vs. CNR and phase threshold ($\gamma_c = 0.99$).

CNR \ η_θ (rad.)	0.5	1	1.5	2	2.5
0 dB	0.6712	0.4281	0.2698	0.1636	0.0846
10 dB	0.2852	0.1082	0.0545	0.0299	0.0148
20 dB	0.0763	0.0227	0.0108	0.0058	0.0029
30 dB	0.0441	0.0127	0.0060	0.0032	0.0016
40 dB	0.0407	0.0117	0.0055	0.0030	0.0015

Table 7. P_{FA} vs. CNR and phase threshold ($\gamma_c = 1$).

CNR \ η_θ (rad.)	0.5	1	1.5	2	2.5
0 dB	0.668692	0.424951	0.267186	0.161782	0.083577
10 dB	0.266857	0.099022	0.049543	0.027129	0.013398
20 dB	0.039964	0.011462	0.005417	0.002910	0.001427
30 dB	0.004215	0.001164	0.000546	0.000293	0.000143
40 dB	0.000423	0.000116	0.000054	0.000029	0.000014

3.2 Probability of Detection

The *pdf* in the presence of target is required for computing the probability of detection P_D . Unfortunately; this *pdf* is not analytically available. A Monte Carlo simulation was used instead. Figure 14 shows the *pdf* plots with 100,000 trials for three different values of signal-to-clutter ratio (SCR), for a CNR value of 20dB and $\gamma_c = 1$, and the interferometric phase induced by the target equal to 2 radians. The corresponding P_D plots vs. the phase threshold are shown in Figure 15. For example, if $\eta_\theta = 1.5$ radians, then $P_D = 0.805$ for SCR = 10 dB and $P_D = 0.024$ for SCR = 0 dB. Therefore, rather high SCR is required for reliable

detection. Recall that (Table 7) the corresponding false alarm rate is $P_{FA} = 5.4 \times 10^{-3}$, which is too high for almost any military radar application.

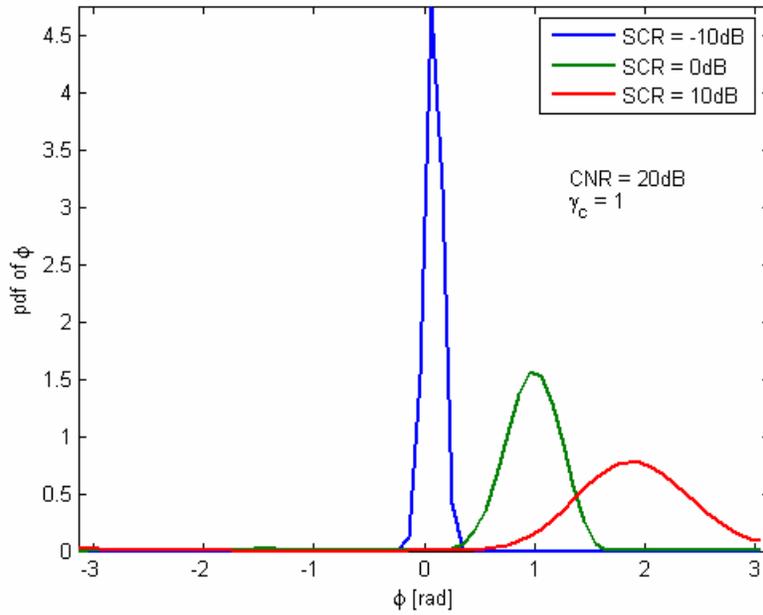


Figure 14. Phase *pdf* for three different SCR values in presence of a moving target.

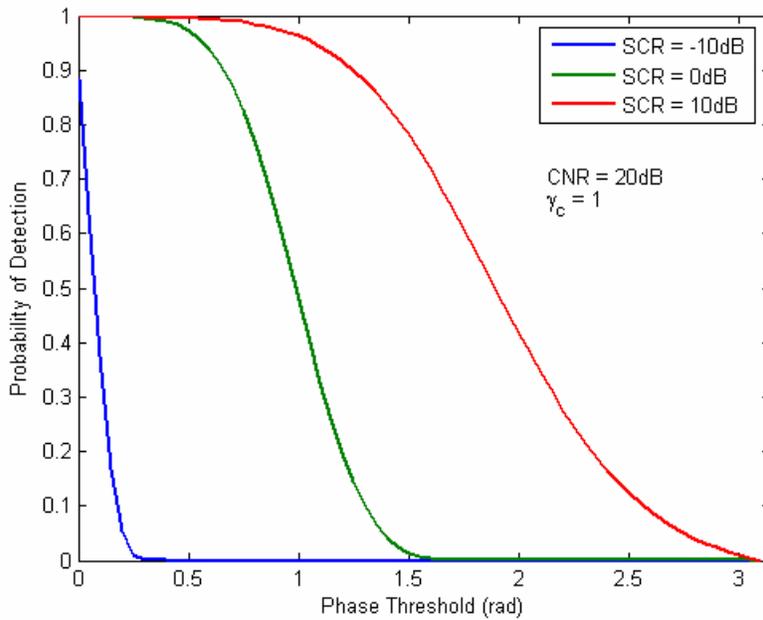


Figure 15. Detection probability for three different SCR values in presence of a moving target.

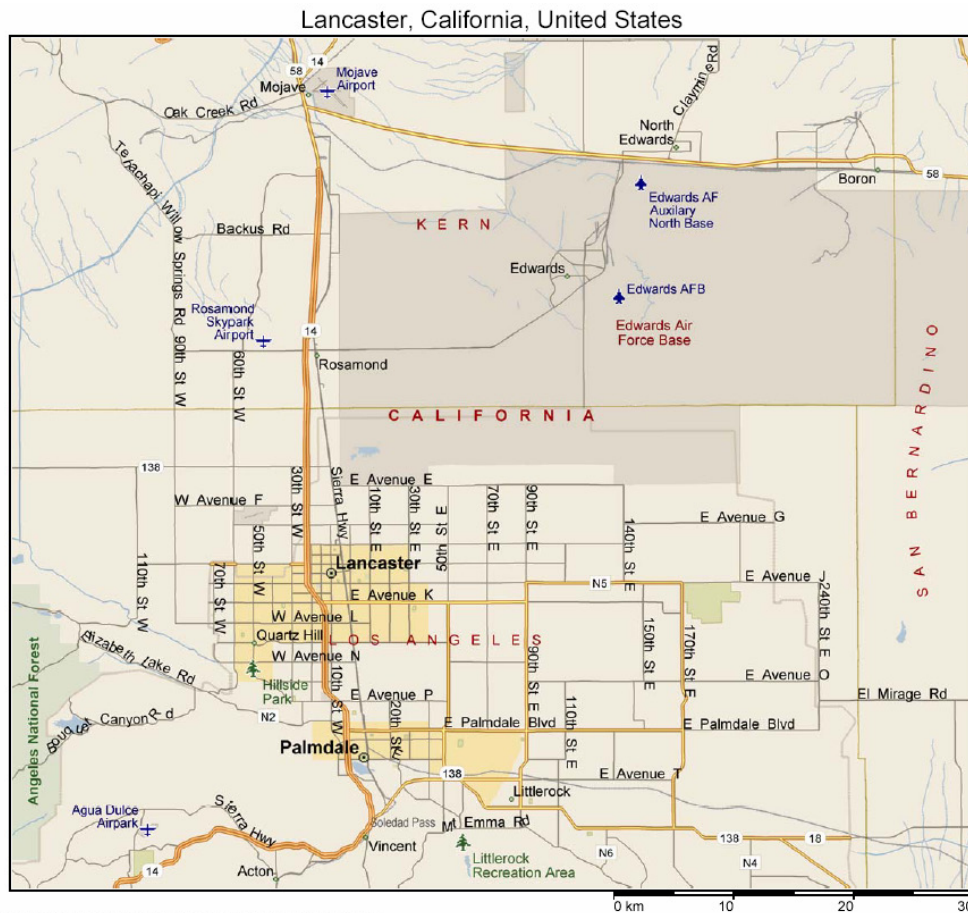
4.0 New C-Band AirSAR ATI Data

4.1 Data and System Parameters

The new AirSAR ATI data provided by JPL recently are collected at C-band in April 2004, in the Lancaster area, CA, as shown in Figure 16. The data we received included three file folders, each including two 2.5GB image data files and many supportive files, as listed in Table 8.

Table 8. Information of received C-band AirSAR ATI data.

File Folder Name	OutCDA06	OutCAB03	OutCZA02
Mode	Ping-pong	Standard	Double baseline
Processing Mode Mnemonic	CDA	CAB	CZA



Copyright © 1998-2003 Microsoft Corp. and/or its suppliers. All rights reserved. <http://www.microsoft.com/streets>
 © Copyright 2002 by Geographic Data Technology, Inc. All rights reserved. © 2002 Navigation Technologies. All rights reserved. This data includes information taken with permission from Canadian authorities © 1991-2002 Government of Canada (Statistics Canada and/or Geomatics Canada), all rights reserved.

Figure 16. Map of Lancaster, CA.

Figure 17 shows the AirSAR instrument (panels behind wing), mounted aboard a modified NASA DC-8 aircraft¹. Typical system and scenario parameters associated with the data are:

- Platform Velocity: $V_p = 214.77$ m
- Platform Height: $H_p = 8.6934$ km
- Average Terrain Height: 662 m
- Baseline Distance: 2.0794 m
- PRF = 546 Hz
- Range at the First Range Bin: $R_{\min} = 8768.93$ m
- Slant Range Spacing: $\Delta R_s = 3.331$ m
- Radar Center Frequency: 5.2875 GHz (Wavelength: $\lambda = 5.67$ cm)
- Chirp Bandwidth: 40 MHz.



Figure 17. AirSAR instrument (panels behind wing) mounted aboard a modified NASA DC-8 aircraft.

¹ More details can be found at http://airsar.jpl.nasa.gov/index_detail.html

4.1.1 “Ping-Pong” Mode

Each SAR data file has a total of 167279 records. Each record includes 2000 complex (8 byte IEEE) range samples. Records are divided into 46 patches/blocks separated by 10 blank records. The sizes (number of records) and the first record indices (“1st Rec #”) of 46 patches are listed as follows:

Patch #	1	2	3	4	5	6	7	8	9	10
Size	6546	3910	3908	3910	3910	3909	670	810	809	809
1 st Rec. #	6	6562	10482	14400	18320	22240	26159	26839	27659	28478

Patch #	11	12	13	14	15	16	17	18	19	20
Size	810	3909	3908	3910	3909	3908	3909	3910	3909	3909
1 st Rec. #	29297	30117	34036	37954	41874	45793	49711	53630	57550	61469

Patch #	21	22	23	24	25	26	27	28	29	30
Size	3909	3910	3909	3909	3910	3909	3909	3908	3910	3909
1 st Rec. #	65388	69307	73227	77146	81065	84985	88904	92823	96741	100661

Patch #	31	32	33	34	35	36	37	38
Size	3909	3910	3910	3910	3908	3909	3910	3908
1 st Rec. #	104580	108499	112419	116339	120259	124177	128096	132016

Patch #	39	40	41	42	43	44	45	46
Size	3909	3908	3908	3908	3909	3908	3908	3908
1 st Rec. #	135934	139853	143771	147689	151607	155526	159444	163362

4.1.2 Standard and Double Baseline Modes

The SAR data for “standard” and “double baseline” modes have the same size and structure. Each SAR data file has a total of 167272 records. Each record includes 2000 complex (8 byte IEEE) range samples. Records are divided into 46 patches/blocks separated by 10 blank records. The sizes (number of records) and the first record indices of 46 patches are listed as follows:

Patch #	1	2	3	4	5	6	7	8	9	10
Size	6543	3910	3909	3910	3910	3909	670	809	810	809
1 st Rec. #	1	6554	10474	14393	18313	22233	26152	26832	27651	28471

Patch #	11	12	13	14	15	16	17	18	19	20
Size	810	3909	3908	3909	3910	3908	3909	3910	3909	3909
1 st Rec. #	29290	30110	34029	37947	41866	45786	49704	53623	57543	61462

Patch #	21	22	23	24	25	26	27	28	29	30
Size	3909	3910	3909	3909	3909	3910	3909	3908	3909	3909
1 st Rec. #	65381	69300	73220	77139	81058	84977	88897	92816	96734	100653

Patch #	31	32	33	34	35	36	37	38
Size	3910	3909	3910	3910	3908	3909	3910	3908
1 st Rec. #	104572	108492	112412	116332	120252	124170	128089	132009

Patch #	39	40	41	42	43	44	45	46
Size	3909	3908	3908	3908	3909	3907	3909	3908
1 st Rec. #	135927	139846	143764	147682	151600	155519	159436	163355

•

4.2 Stripmap SAR Images

4.2.1 Cross-Range Resolution

The cross-range resolution for focused aperture stripmap SAR can be expressed [13] as

$$\Delta R_c = \frac{\text{PRF} \cdot R \lambda}{2N V_p} \quad (25)$$

where N is the pulse number in a coherent processing interval (CPI) and R is the slant range.

Table 9 lists some results for PRF = 546 Hz, $V_p = 214.77$ m, and $\lambda = 5.67$ cm. It is usually desirable to maintain a square resolution in stripmap SAR mode [13]. Because the slant range resolution in JPL's C-band AirSAR data is 3.33m, N = 256 pulses in a CPI may be a good choice for this example from Table 9. Therefore, 256 pulses will be used for SAR image processing in this report if not otherwise specified.

Table 9. Cross-range resolution (ΔR_c) in meters.

Slant Range	$R_{\min} = 8768.93 \text{ m}$	$R_{\max} = 15430.99 \text{ m}$
N = 1024	0.62	1.09
N = 512	1.23	2.17
N = 256	2.47	4.34

4.2.2 SAR Images

Because all data of three modes are recorded in the same scenario, they produce similar SAR images. This report only presents the results from one data file, recorded on the Antenna 1 in the folder: OutCDA06 (“ping-pong” mode). A line-by-line direct-convolution method is used for the stripmap SAR imaging with $N = 256$ pulses in a CPI, which leads to a square resolution. Figure 18 shows the SAR images (in dB with 80dB of dynamic range) for 42 patches. Because there are too few records in patches 7 through 11, they are ignored here. The AirSAR radar starts recording Patch 1 from the area of Mojave Airport, CA, and then down south along Route 14. Comparing the SAR images from Patch 1 to Patch 13 with Figure 19, newly taken bird-eye picture in the area of Mojave Airport, we can see that the SAR images match the picture very well.

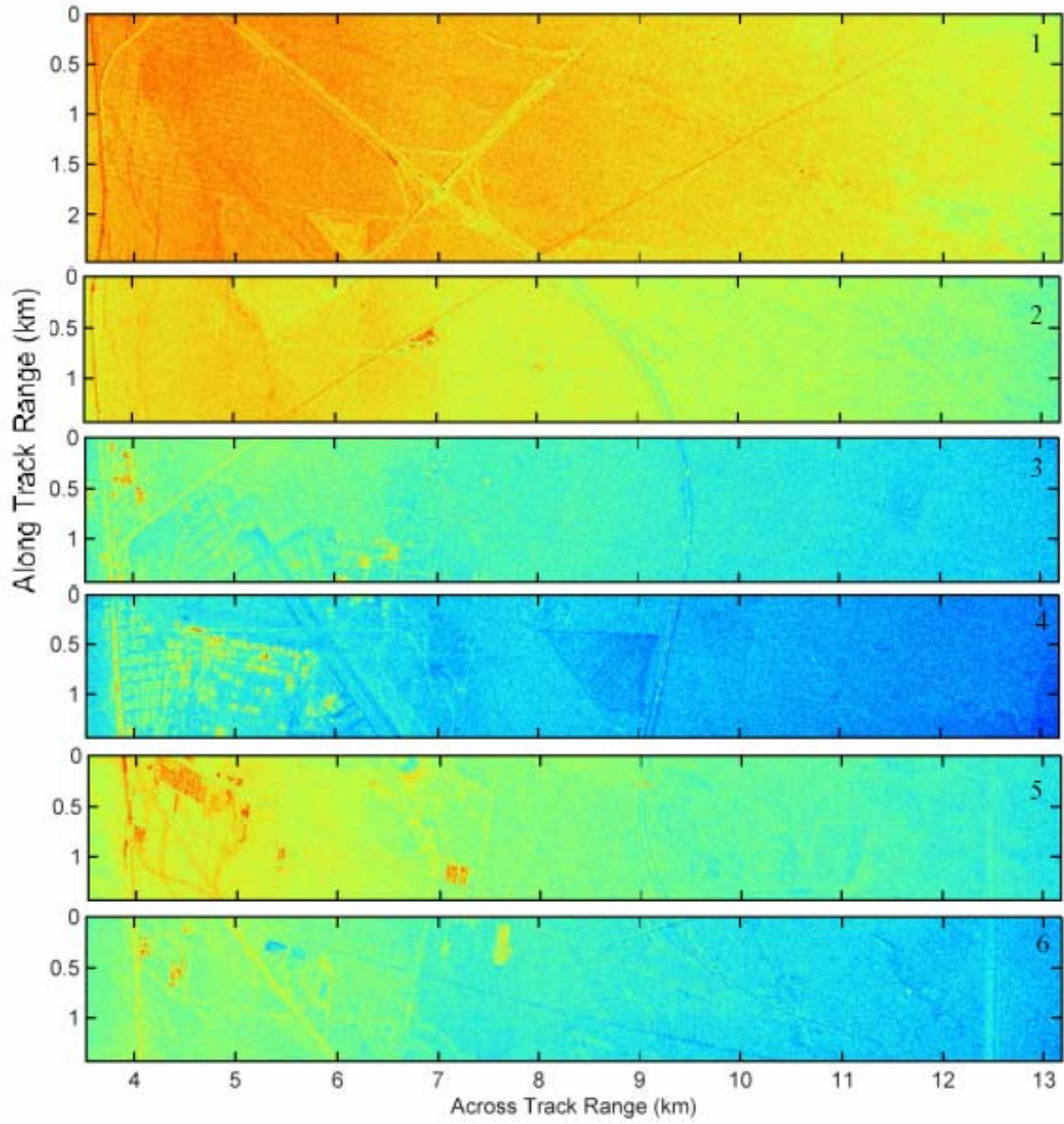


Figure 18. Stripmap SAR images using the C-band AirSAR data. Cont.)

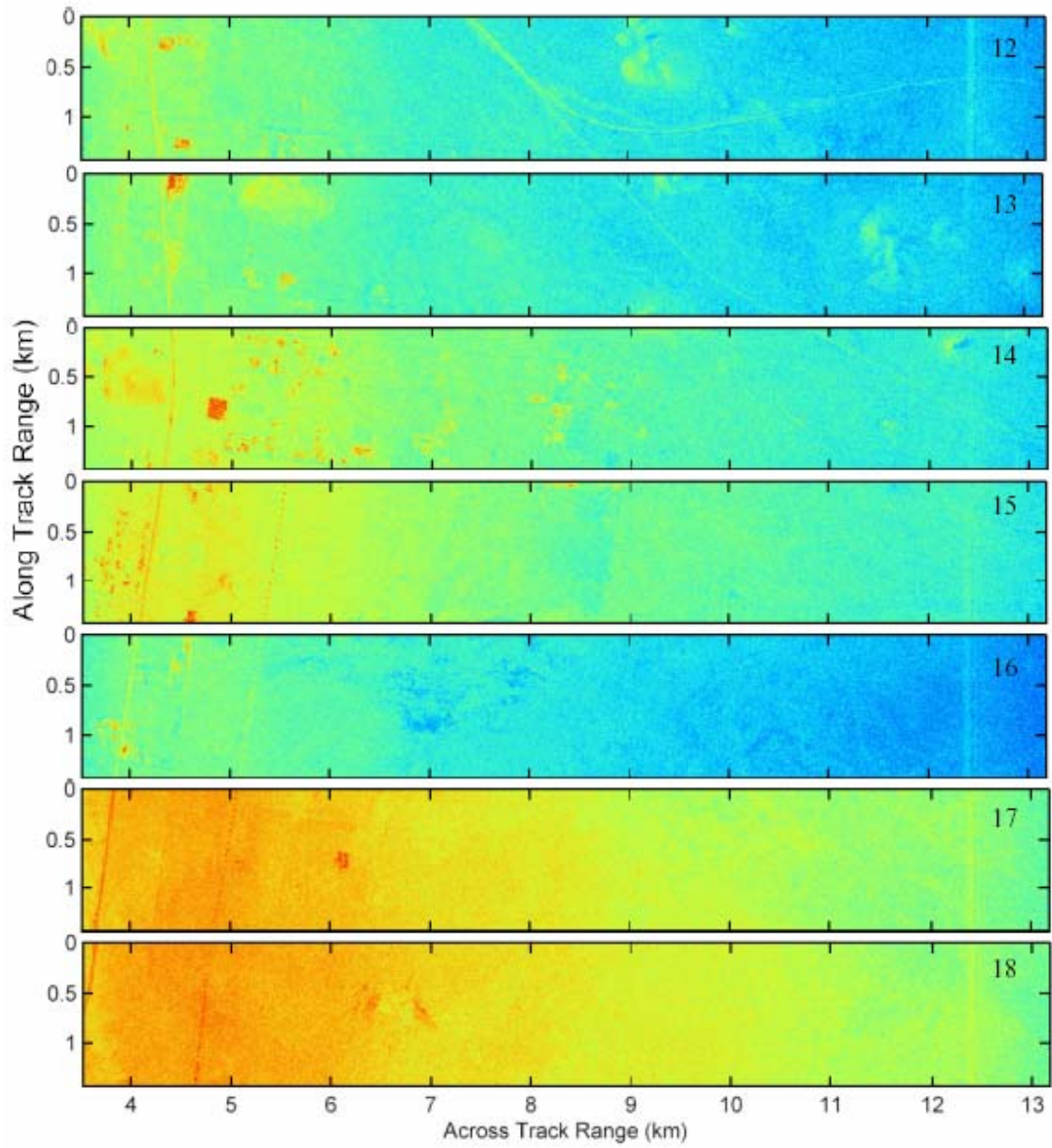


Figure 18. Stripmap SAR images using the C-band AirSAR data.(Cont.)

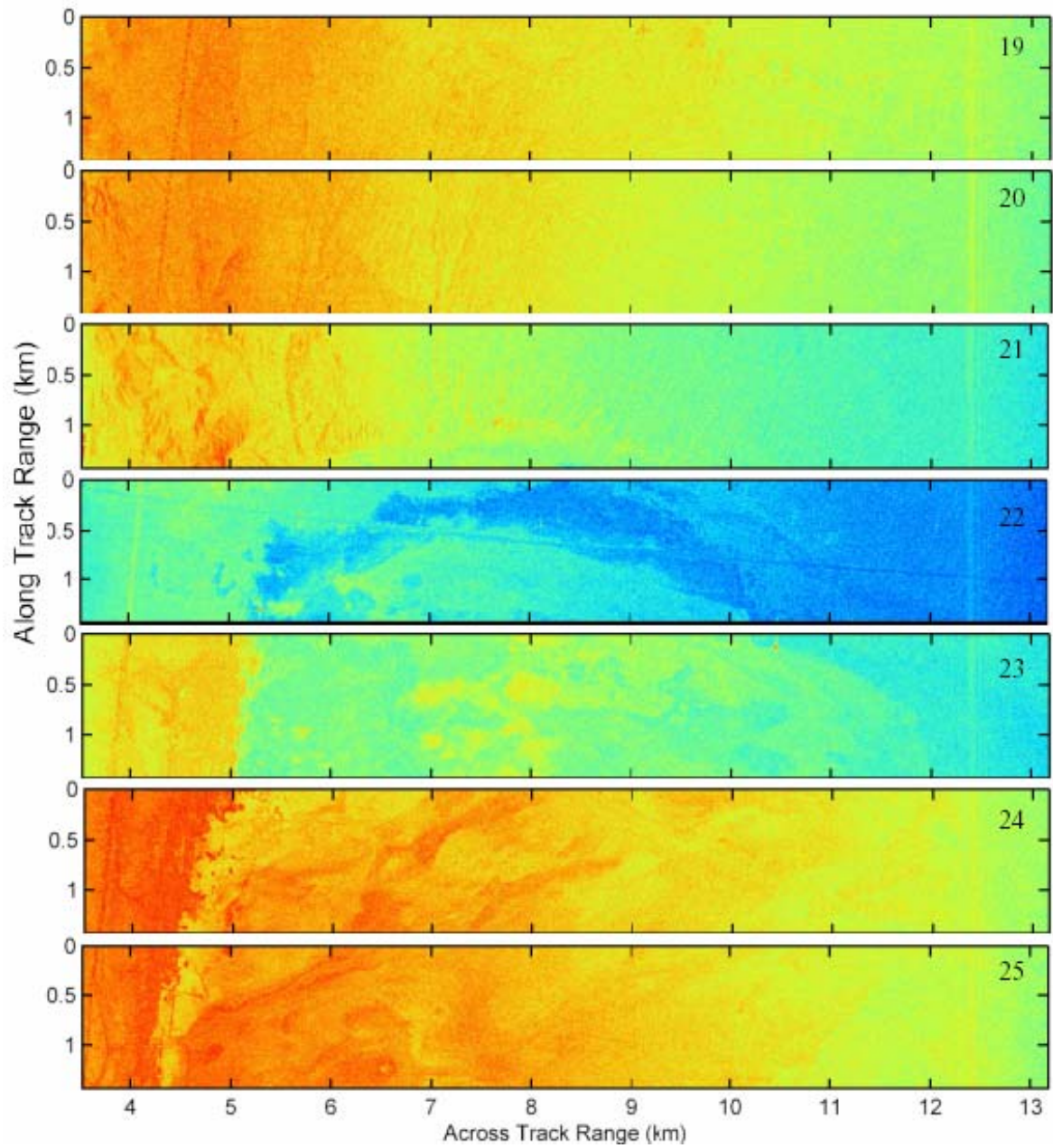


Figure 18. Stripmap SAR images using the C-band AirSAR data.(Cont.)

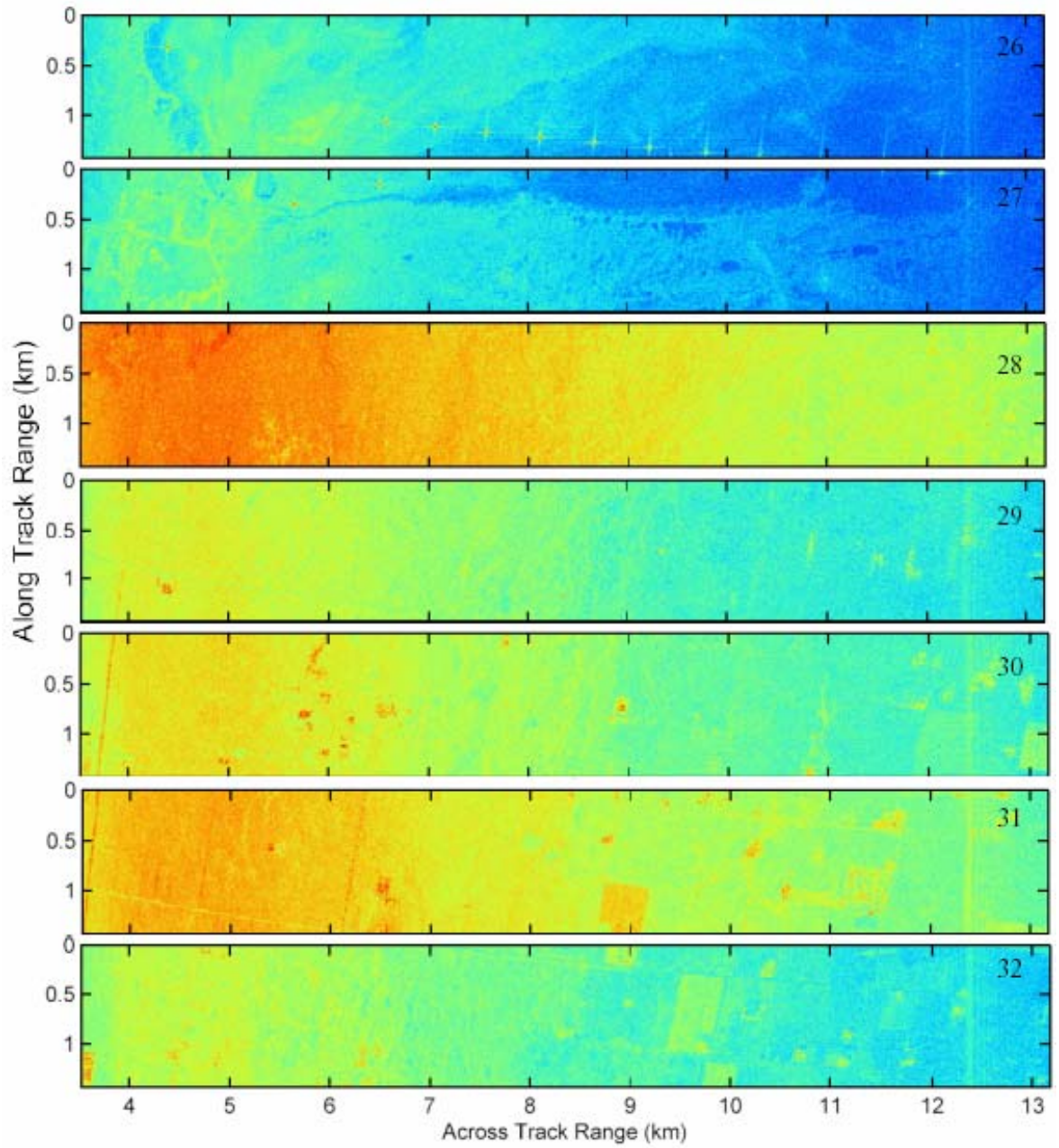


Figure 18. Stripmap SAR images using the C-band AirSAR data.(Cont.)

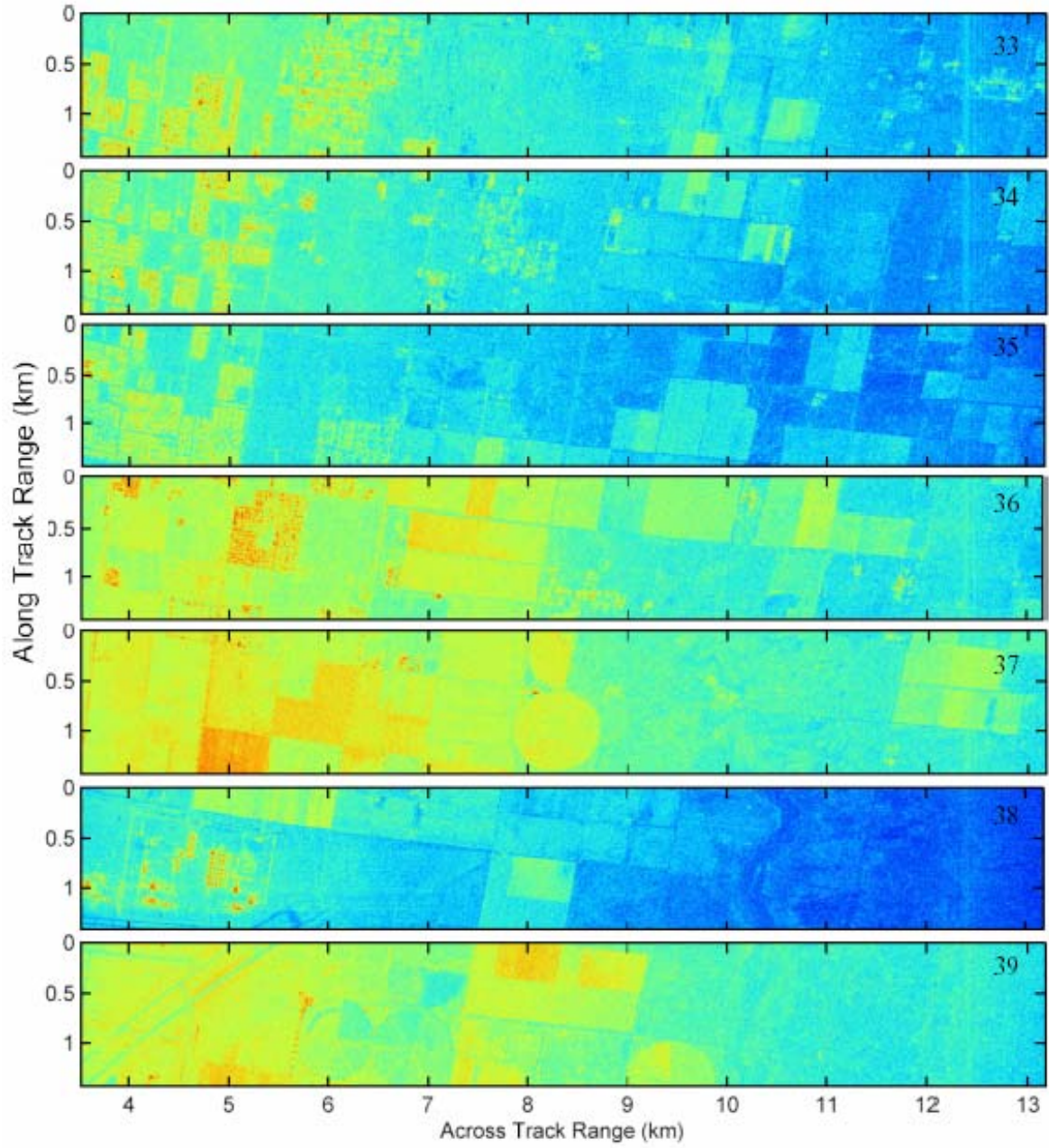


Figure 18. Stripmap SAR images using the C-band AirSAR data.(Cont.)

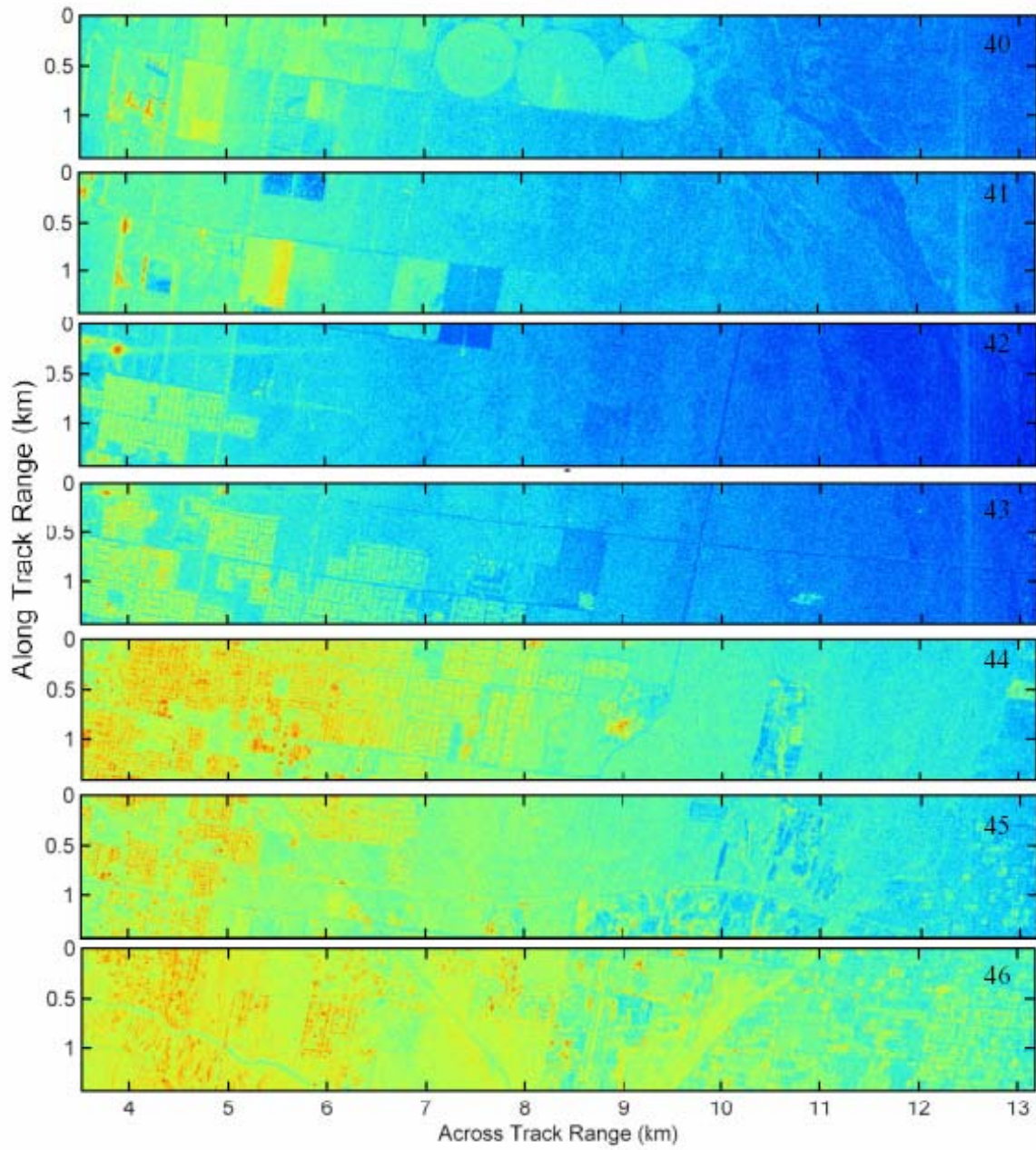


Figure 18. Stripmap SAR images using the C-band AirSAR data.



Figure 19. Newly taken bird-eye picture in the area of Mojave Airport, CA.

5.0 Blind Calibration for Group Phase Shift Induced by Crab Angle

5.1 Group Phase Shift Induced by Crab Angle

In the ideal case, two ATI-antennas are aligned with the moving track. However, the crabangle (yaw and pitch) makes one antenna offset from the moving track of the other.

Figure 20 illustrates a case where the platform has a yaw angle θ_c , which leads to an offset distance in cross-track direction:

$$\Delta y = B_x \sin \theta_c, \quad (26)$$

where B_x is the baseline distance. The cross-track offset of two-antennas will induce a phase shift between Images A and B, called group phase shift in this report, which must be calibrated before the ATI-SAR processing. Because the platform's crab angle varies during its motion [10], the group phase shift will vary with pixels along the track. Moreover, we can show that the group phase shift also rapidly varies with slant range.

From the scenario in Figure 20, we can express the path difference from a ground point P (with zero Doppler) to two antennas as

$$\Delta r \approx \Delta y \cos \phi = B_x \sin \theta_c \cos \phi = B_x \sin \theta_c \sqrt{1 - (H/R)^2} \quad (27)$$

where ϕ is the grazing angle at Point P, H is the platform height from the local earth ground, and R is the slant range from P to the middle of two antennas.

In the “ping-pong” mode, the group phase shift due to the path difference will be

$$\Delta \varphi = \frac{4\pi}{\lambda} \Delta r = \frac{4\pi}{\lambda} B_x \sin \theta_c \sqrt{1 - (H/R)^2}, \text{ for “ping-pong” mode.} \quad (28)$$

Similarly, the group phase shifts in “standard” and “double baseline” modes can be expressed as

$$\Delta \varphi = \frac{2\pi}{\lambda} B_x \sin \theta_c \sqrt{1 - (H/R)^2}, \text{ for “standard” mode} \quad (29)$$

and

$$\Delta\phi = \frac{4\pi}{\lambda} V_p T \sin \theta_c \sqrt{1 - (H/R)^2}, \text{ for "double baseline" mode.} \quad (30)$$

Using the parameters given in subsection 4.1, Figure 21 shows the group phase shift as a function of pixel's slant range with yaw angle equal to 5° and 10° . Figure 22 compares the group phase shifts of three modes when the yaw angle is equal to 5° . It is shown that the group phase shift varies rapidly with the pixel's slant range for all three modes. The phase variation rate with range is the fastest in "ping-pong" mode, and the slowest in "double baseline" mode. Therefore, a two-dimensional (along track and across track) interferometric phase calibration is necessary before further ATI-SAR processing.

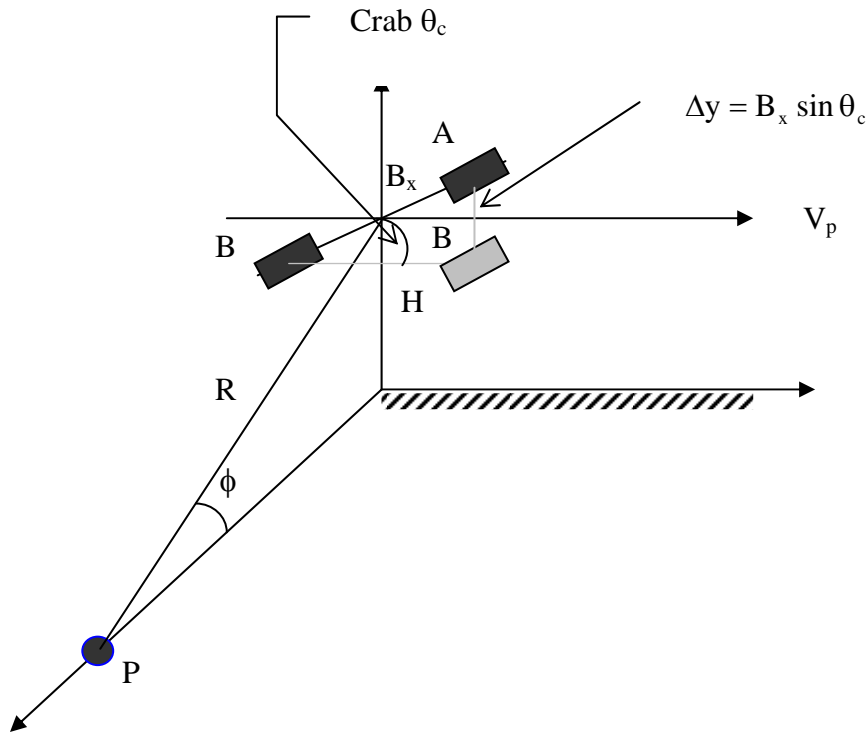


Figure 20. Across-track offset between two antennas induced by the crab (yaw) angle.

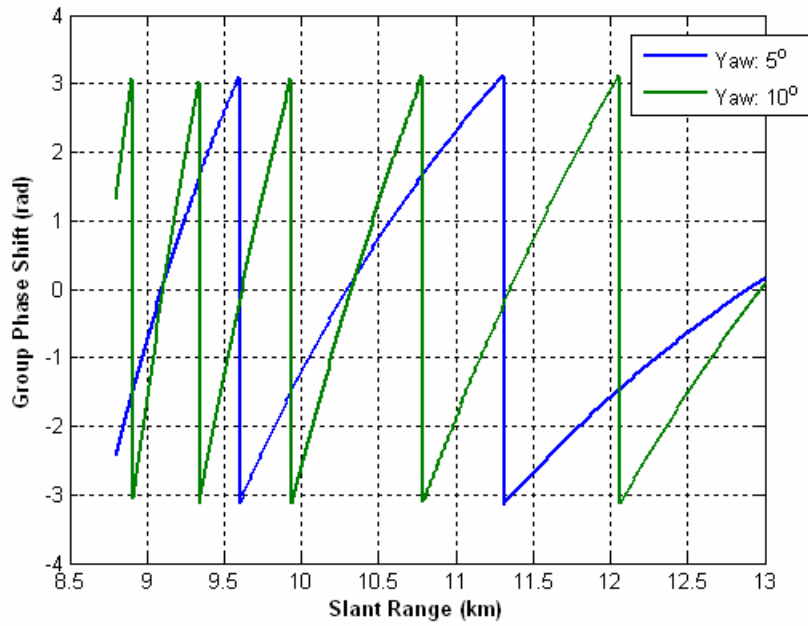


Figure 21. Group phase shift induced by yaw angle as a function of slant range (“ping-pong” mode).

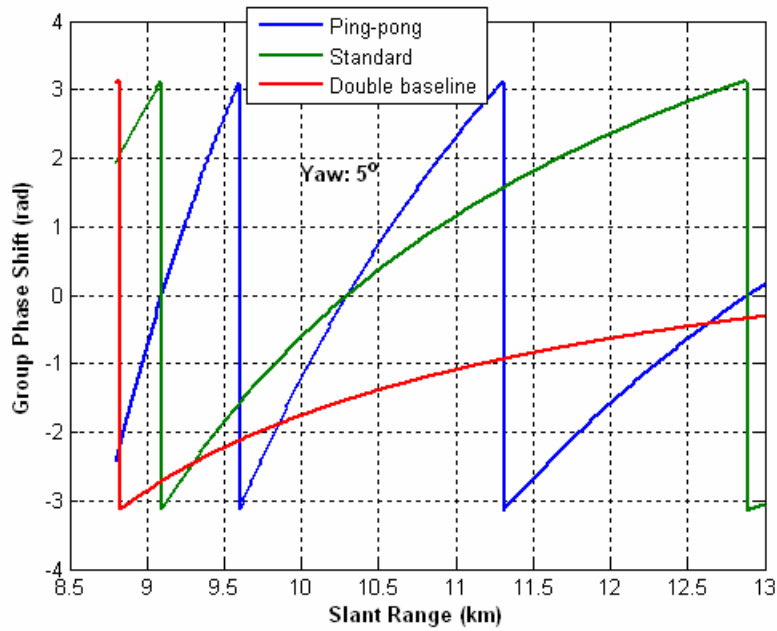


Figure 22. Group phase shift induced as a function of slant range (Yaw: 5°).

5.2 Two-Dimensional Blind Calibration for Interferometric Phase

Reference [10] developed a calibration method based on the INU-measured attitude data and an array of known stationary corner reflectors (strong scatterers) as a reference. This report proposes a blind calibration method that does not require any knowledge of the attitude and ground reference scatterers. This method tries to estimate the group phase shift as a function of pixel's position, and then calibrate the interferometric phase map.

As discussed in the previous section, the group phase shift varies with the slant range as well as the cross-range. It is difficult to estimate the two-dimensional phase shift without further information. In this report, we assume that the crab angle varies slowly with time.

Particularly, we assume that the crab angle remains the same in adjacent N_1 records, which is corresponding to the platform flight distance: $N_1 V_p / \text{PRF}$. For example, the flight distance is about 80m for $N_1 = 200$, $V_p = 215$ m/s, and $\text{PRF} = 546$ Hz. Thus, we will divide the interferometric phase map into groups first, each including N_1 cross-range pixels. Then, we estimate and calibrate the group phase shift as a function of slant range for each group. It is found that one estimation and calibration is not enough, because the estimation of group phase shift is based on wrapped interferometric phases (in $[-\pi, \pi]$), and the compensated phases are wrapped again which leads to a new group phase shift. An iterative procedure is used in this report, instead.

Assume that the size of the interferometric phase map to be calibrated is $N_s \times N_c$, where N_s is the number of pixels in the slant range dimension and N_c is the number of pixels in the cross-range dimension. The proposed calibration method is described in the following steps:

1. Divide the interferometric phase map into $\lceil N_c / N_1 \rceil$ groups, each with size $N_s \times N_1$ except for the last one, which includes the remaining ($< N_1$) cross-range pixels.
2. For each group, estimate and calibrate the group phase shift as a function of slant range.

There are many possible estimation methods. Our proposed method is described in the following:

1. For each slant range cell, sort the interferometric phases of N_1 cross-range pixels
2. Take the mean of 10 middle phases as the estimation of the group phase shift for the corresponding slant range cell.
3. Compute the mean and standard deviation of the estimated group phase shift (over slant range cells). The mean and standard deviation in the ideal case are zero. If they are small enough, no further calibration is necessary, and go to Step 3.
4. Compensate the phase shift by subtracting the estimated group phase shift, and wrap the results within $[-\pi, \pi]$.
5. Back to Step 1).
6. Back to Step 2 for next group.

5.3 In Illustration Example

To illustrate the problem of group phase shift and the proposed calibration method, we have selected a partial area (500 slant range cells) from Patch 3 in “OutCDA06”, as shown in Figure 23 for the SAR image of selected area.

Figure 24 shows the interferometric phase map for the SAR image shown in Figure 23 before phase calibration. Obviously, the phases of most pixels are far from zero, as shown in Figure 25 for the histogram of interferometric phase before phase calibration.

Figure 26 shows the interferometric phase image after the phase calibration using the proposed blind calibration method. Clearly, the phases of most pixels are close to zero after the calibration, as shown in Figure 27 for the corresponding histogram of interferometric phase after the calibration.

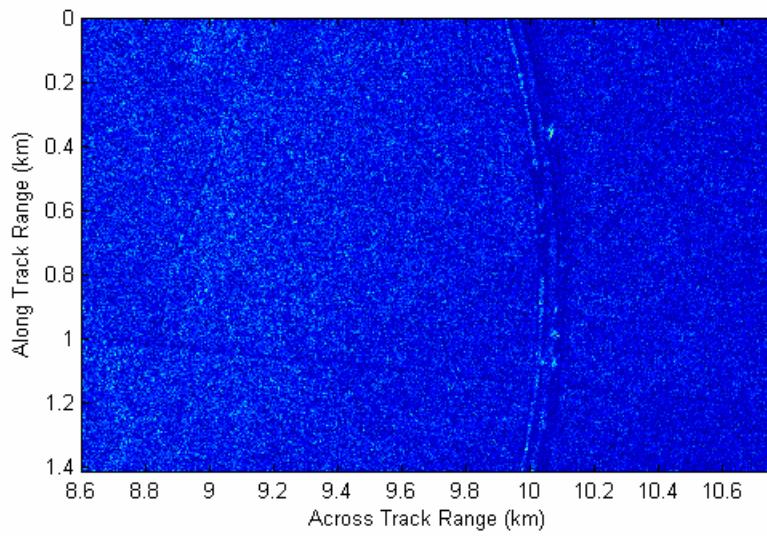


Figure 23. Image A for selected area (from Patch 3).

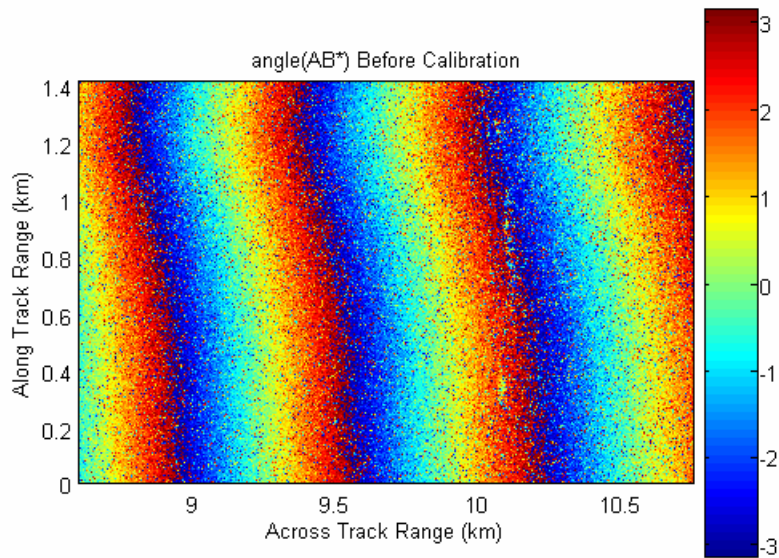


Figure 24. Interferometric phase map before the phase calibration for crab angle.

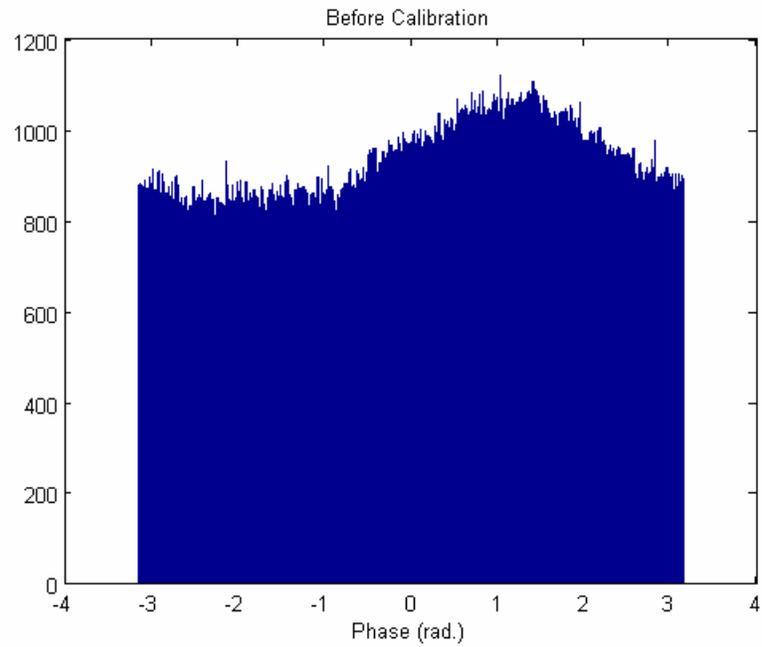


Figure 25. Histogram of interferometric phase before phase calibration.

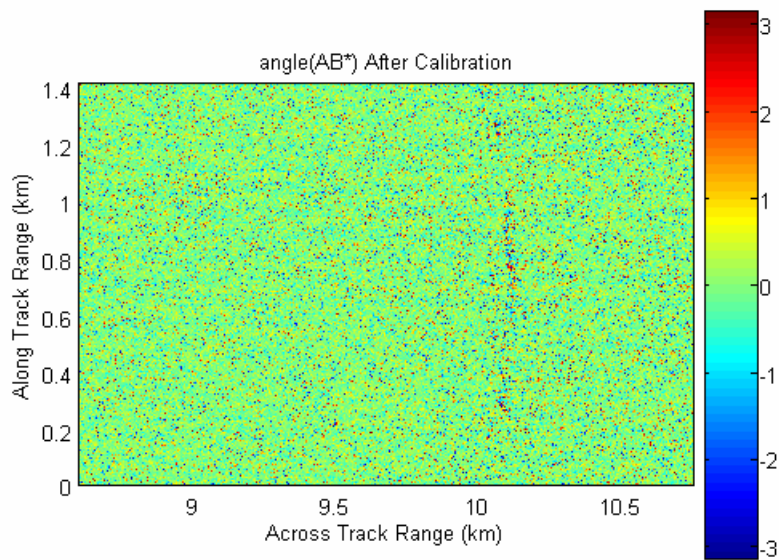


Figure 26. Interferometric phase map after the phase calibration.

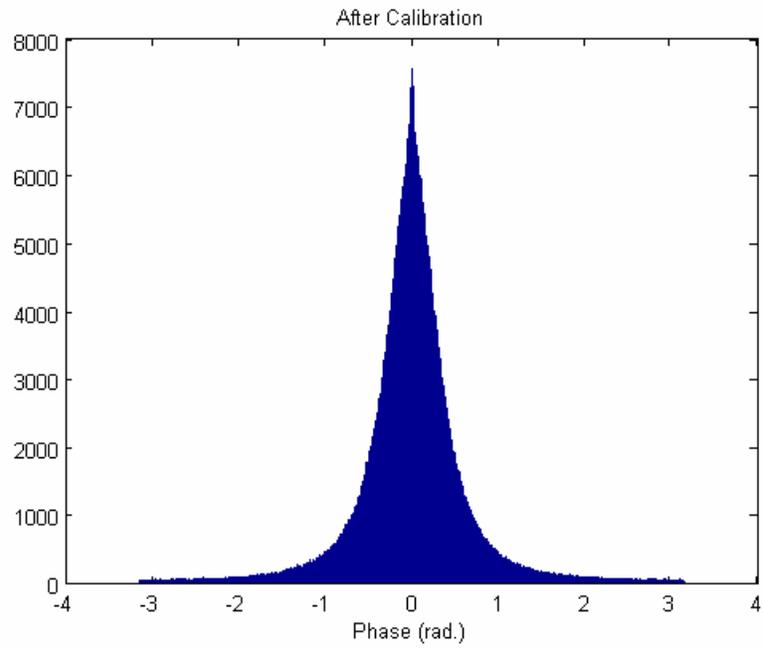


Figure 27. Histogram of interferometric phase after the phase calibration.

6.0 Moving Target Detection Using ATI-SAR

In this section, we still use the selected partial area, as shown in Figure 23, from Patch 3 in OutCDA06 (“ping-pong” mode), except where otherwise specified.

6.1 Phase-Only Detection

Phase-only detection is the conventional ATI-SAR method. Denote η_0 as the phase threshold. The phase at any pixel below the threshold will be forced to zero. Figure 28 shows the results with $\eta_0 = 1$ radian. Obviously, the false alarm rate is too high for radar applications involving Ground Moving Target Indication (GMTI).

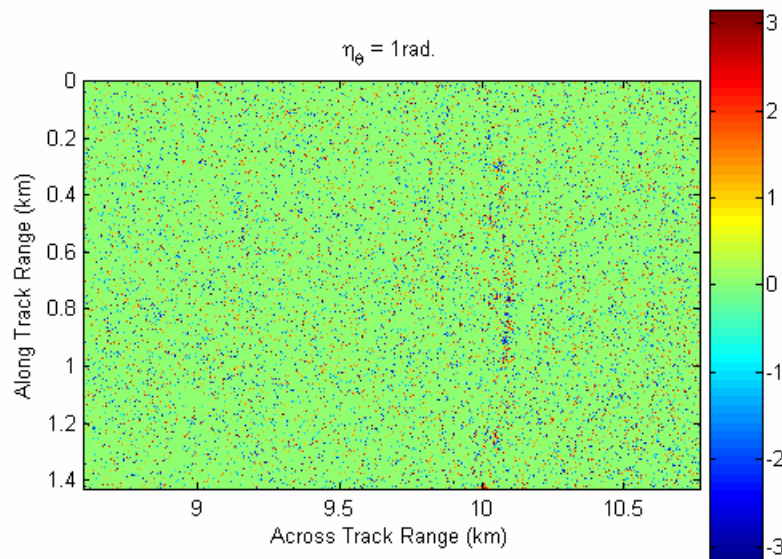


Figure 28. Interferometric phase map with $\eta_0 = 1$ radian.

6.2 Amplitude-Only Detection

The amplitude-only detection suppresses the weak pixels from large smooth surfaces such as road and water surfaces. This detection is similar to the conventional constant false alarm rate (CFAR) processing. There are many algorithms available in the literature to determine the threshold [15]. The performance depends on the environment. As an example, the

threshold is counted relative to the mean amplitude for background in this report, which is estimated by taking the root mean square (rms) mean value of the median amplitudes (of the corresponding slant-range pixels) over cross-range pixels.

Figure 29 shows the SAR amplitude image trimmed with an amplitude threshold ($\eta_a = 6\text{dB}$) only. This image shows stronger pixels that could possibly contain moving targets, stationary objects, and other discretely. The amplitude-only detection suppresses the weak pixels such as those corresponding to road and water surfaces, but it can not separate the moving targets from the stationary background.

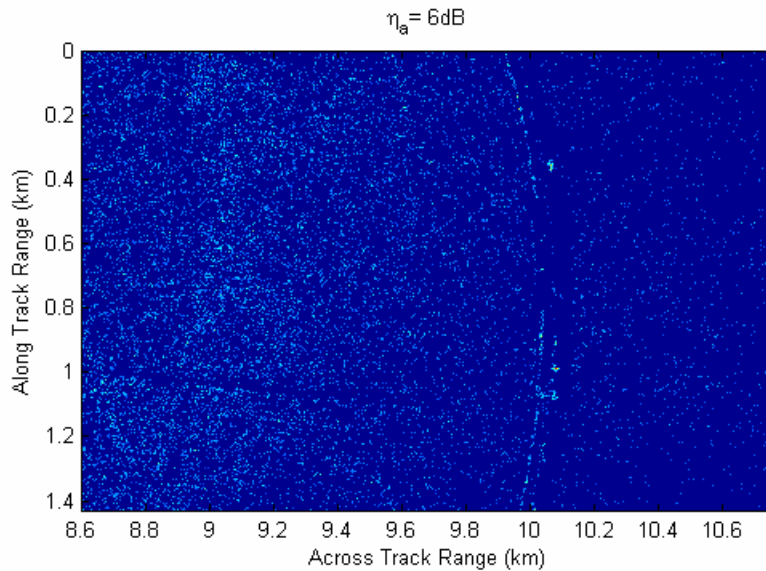


Figure 29. SAR amplitude image with $\eta_a = 6\text{ dB}$.

6.3 Dual-Threshold Detection

In this effort, we propose to combine the above-mentioned amplitude-only detection with the phase-only detection. Using the two thresholds (phase and amplitude), we get two outputs:

An interferometric phase map (target velocity) is obtained by applying the interferometric phase detection only to the pixels selected by the amplitude detection. Specifically, the phase at a pixel will be forced to zero if its image amplitude is below a pre-determined threshold.

And,

An amplitude map (target strength) is obtained by applying the amplitude detection only to the pixels selected by the interferometric phase detection.

Figure 30 shows the results of the interferometric phase map obtained by applying the amplitude detection results of Figure 29 onto those of Figure 28, i.e., forcing the phase at a pixel to zero if its amplitude is less than the mean value by an amplitude threshold ($\eta_a = 6$ dB here). Clearly, the false alarm rate is dramatically reduced using this approach.

Similarly, we can obtain an amplitude map of potential moving targets by applying the phase detection results of Figure 28 onto those of Figure 29, i.e., eliminating the pixels whose phases are below the phase threshold ($\eta_\theta = 1$ radian here), as shown in Figure 31, which corresponds to the interferometric phase map of Figure 30. In other words, Figures 30 and 31 show velocity and strength information of potential moving targets. The locations shown in these Figures are shifted from their real ones due to the SAR processing. It is possible to restore the real locations of those slow targets without any interferometric phase ambiguity. Figure 32 further combines the detection results with the original SAR image. The red points along the road/highways are potential targets (moving vehicles). The red points may have shifted from the road tracks due to the fact that a moving target appears in a SAR image at an apparent position shifted in the along-track direction from its true position.

The road is almost in parallel with the flight track of the radar platform. Therefore, the moving vehicles on that road should have very low radial speed. The fact that many targets on that road are detected shows the extraordinary detection capability of the ATI-SAR approach to slow moving targets.

A MATLAB file, DT_ATR_SAR.m, is given in Appendix 3.1 for demonstrating the results shown in this section.

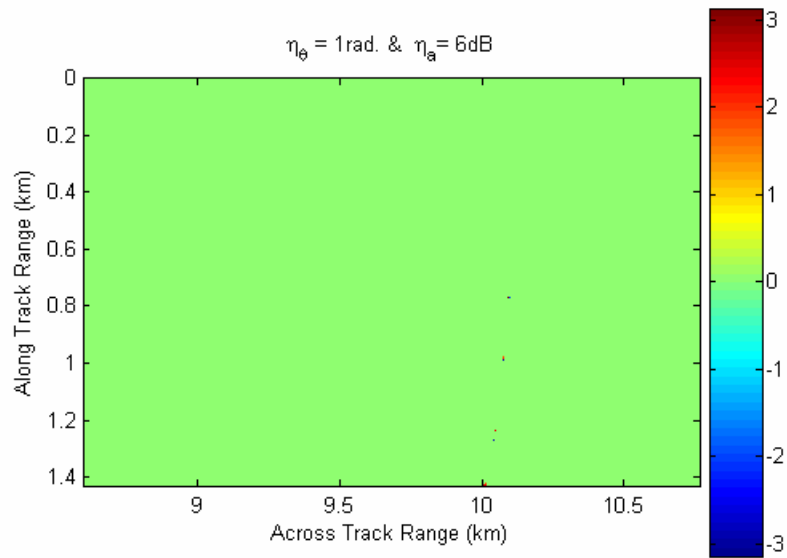


Figure 30. Interferometric phase map with $\eta_\theta = 1$ radian and $\eta_a = 6$ dB .

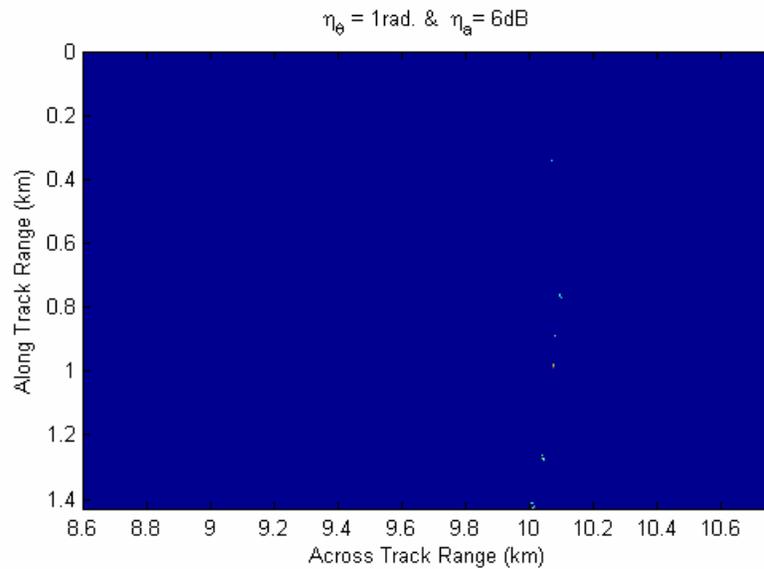


Figure 31. Amplitude map with $\eta_\theta = 1$ radian and $\eta_a = 6$ dB .

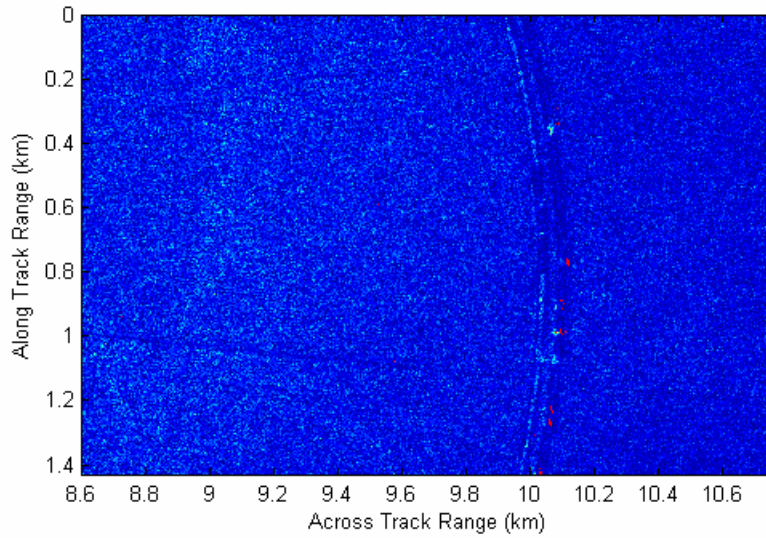


Figure 32. Positions of potential targets (red points) on the SAR image (“ping-pong”).

6.4 Applying the Dual-Threshold Approach to Other ATI-Mode Data

The above demonstration example is based on the “ping-pong” mode data. In this subsection, we will repeat the above study using the “standard” and “double-baseline” mode data, taken from file folders “OutCAB03” and “OutCZA02”, respectively, in the same area as shown in Figure 23.

6.4.1 “Standard” Mode Data

This mode is similar to the “ping-pong” mode, but with higher MDV as shown in Table 4.

Figure 33 shows the interferometric phase map after phase-only detection with

$\eta_{\theta} = 1$ radian. Figure 34 shows the SAR amplitude image trimmed with an amplitude

threshold ($\eta_a = 6$ dB) only. Figures 35 and 36 show the interferometric phase map and the amplitude map of detected targets using joint amplitude and phase detection, respectively.

Figure 37 shows the detection results on the original SAR image. Compared with Figure 32,

we can see similar results but several slower targets are missed because of the higher MDV in the “standard” mode.

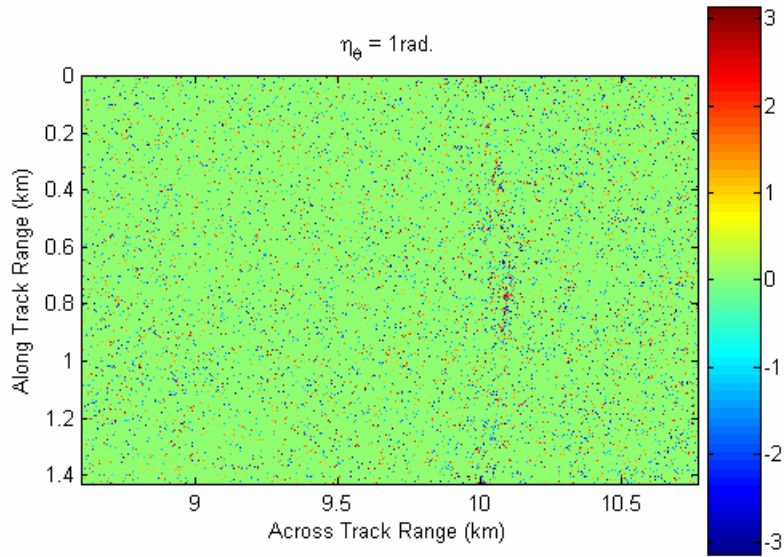


Figure 33. Interferometric phase map with $\eta_\theta = 1$ radian (“standard”).

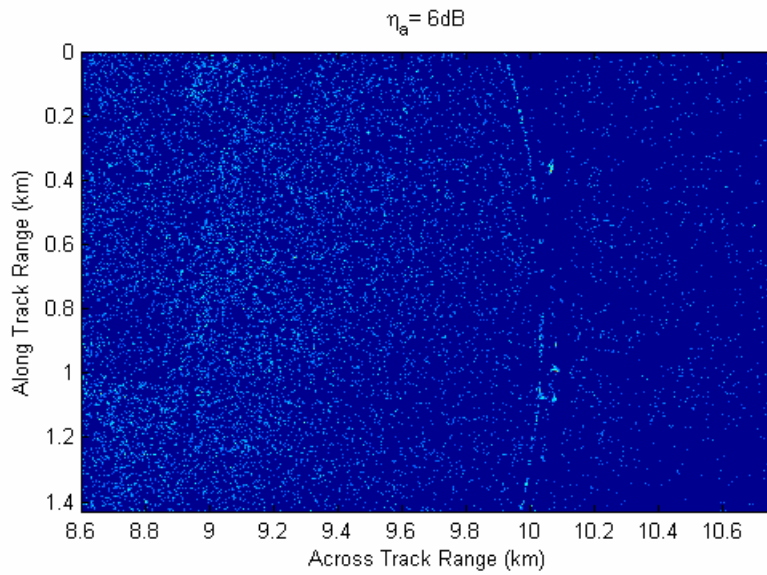


Figure 34. SAR amplitude image with $\eta_a = 6$ dB (“standard”).

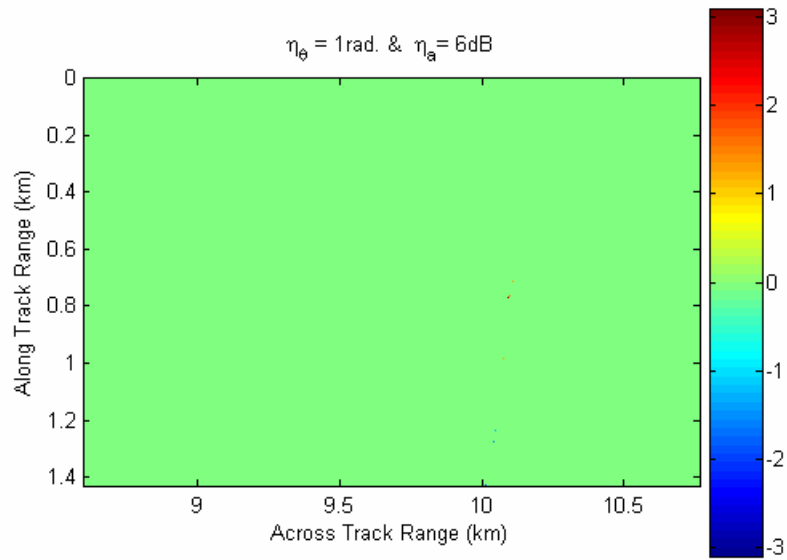


Figure 35. Interferometric phase map with $\eta_\theta = 1$ radian and $\eta_a = 6$ dB (“standard”).

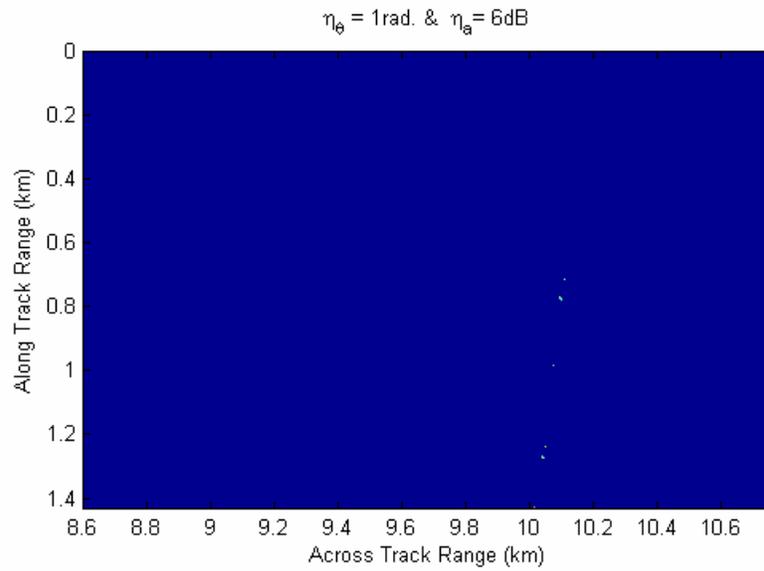


Figure 36. Amplitude map with $\eta_\theta = 1$ radian and $\eta_a = 6$ dB (“standard”).

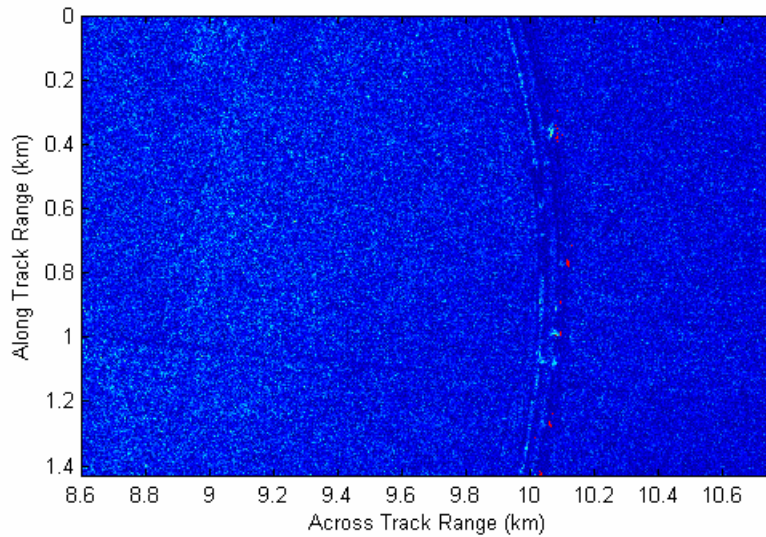


Figure 37. Positions of potential targets (red points) on the SAR image (“standard”).

6.4.2 “Double Baseline” Mode

This mode has the worst MDV as shown in Table 4. Figure 38 shows the interferometric phase map after phase-only detection with $\eta_0 = 1$ radian. Figure 39 shows the SAR amplitude image trimmed with an amplitude threshold ($\eta_a = 6$ dB) only. It is shown that both phase-only and amplitude-only detections produce a very high false alarm rate, just as those seen in the “ping-pong” mode and “standard” mode. Figures 40 and 41 show the interferometric phase map and the amplitude map of detected targets, respectively, using joint amplitude and phase detection. Figure 42 shows the detection results on the original SAR image. Compared with Figure 32, we can see that most targets, detected in the “ping-pong” and “standard” modes, have disappeared because the “double baseline” mode can only detect high radial speed targets.

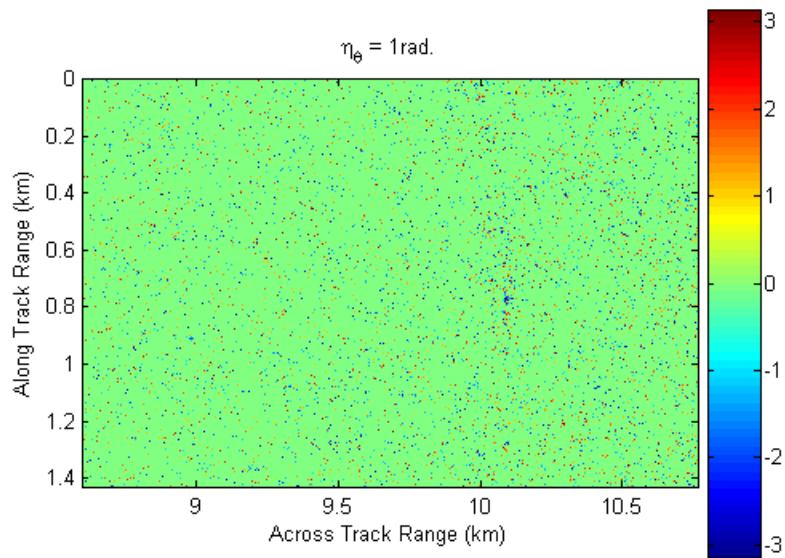


Figure 38. Interferometric phase map with $\eta_\theta = 1$ radian (“double baseline”).

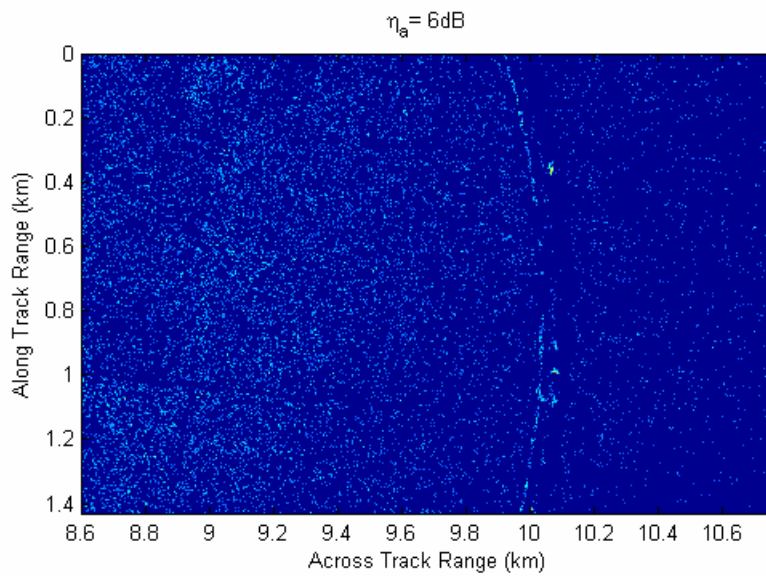


Figure 39. Amplitude image with $\eta_a = 6$ dB (“double baseline”).

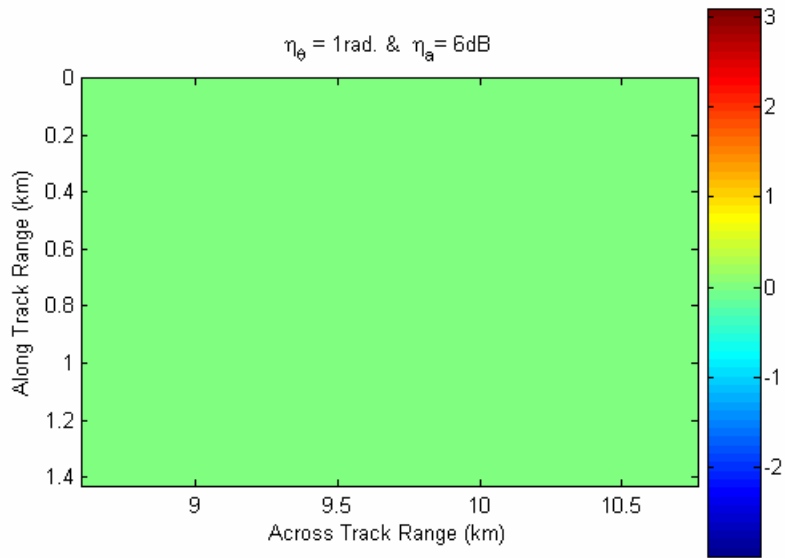


Figure 40. Interferometric phase map with $\eta_\theta = 1$ radian and $\eta_a = 6$ dB (“double baseline”).

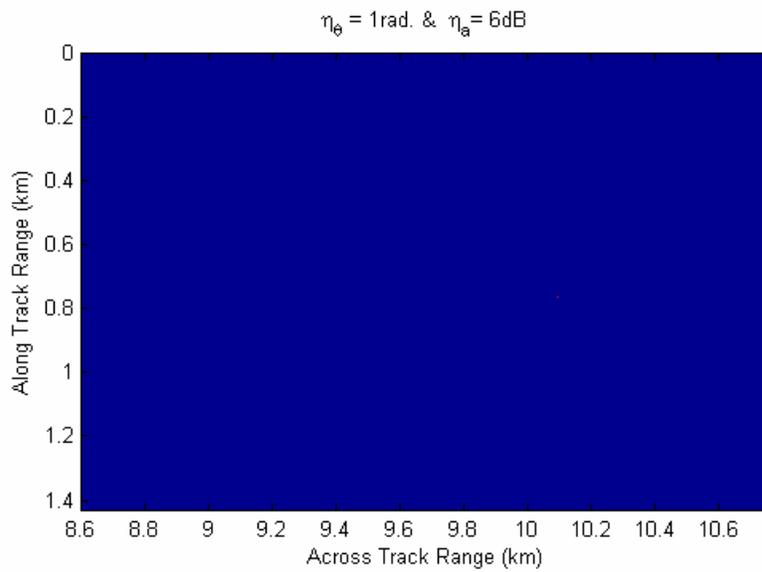


Figure 41. SAR Amplitude map with $\eta_\theta = 1$ radian and $\eta_a = 6$ dB (“double baseline”).

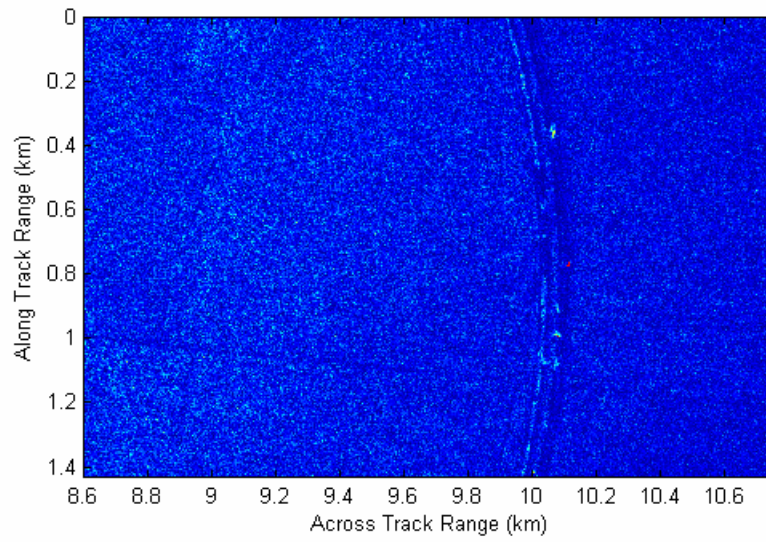


Figure 42. Positions of potential targets (red points) on the SAR image (“double baseline”).

7.0 Conclusions

Conventional ATI-SAR approaches can detect targets with very low radial speeds, but their false alarm rate is too high to be used in GMTI radars. The proposed dual-threshold approach, which combines the conventional interferometric phase detection and the SAR image amplitude detection, can effectively reduce the false alarm rate. The concept of the dual-threshold approach is illustrated using JPL's AirSAR ATI data. A simple two-dimensional blind-calibration procedure is proposed to correct the group phase shift induced by the platform's crab angle. However, the work presented in this report is only our very early effort in this area. Future work would include: (1) completing the dual-threshold detection theory with performance analysis that leads to an easy determination of thresholds; (2) further work with the AirSAR ATI data, including the completion of blind-calibration method, comparative studies in different modes with more sample images, especially those images with known targets; (3) assessing the SAR-MTI algorithm suggested in [16] using the AirSAR data; (4) modifying the dual-threshold approach by replacing the SAR amplitude detection with the SAR-MTI detection.

8.0 Reference

- [1] L. E. Brennan and I. S. Reed, "Theory of adaptive radar," *IEEE Trans. on Aerospace and Electronic Systems*, vol. 9, no. 2, pp. 237-252, March 1973.
- [2] S.M. Kogon, D.J. Rabideau, R.M. Barnes, "Clutter mitigation techniques for space-based radar", *Proceedings IEEE ICASSP*, pp.2323-2326, Phoenix, AZ, March 15-19,1999.
- [3] Y. Zhang and A. Hajjari, "Bistatic space-time adaptive processing (STAP) for airborne/spaceborne applications— signal modeling and simulation tool for multichannel bistatic systems (SMS-MBS)," *Air Force Research Laboratory Final Technical Report*, AFRL-SN-RS-TR-2002-201, Part II, August 2002.
- [4] H. Wang and L. Cai, "On adaptive spatial-temporal processing for airborne surveillance radar systems," *IEEE Transactions on Aerospace and Electronic Systems*, vol. 30, no. 3, pp. 660-670, 1994.
- [5] Y. Zhang and B. Himed, "Effects of geometry on clutter characteristics of bistatic radars," *Proc. 2003 IEEE Radar Conf.*, pp.417-424, Huntsville, AL, May 5-8, 2003.
- [6] Y. Zhang, A. Hajjari, L. Adzima, and B. Himed, "Adaptive beam-domain processing for space-based radars," *Proc. IEEE 2004 Radar Conf.*, Philadelphia, PA, April 26-29, 2004.
- [7] R.M. Golstein and H. A. Zebker, "Interferometric radar measurements of ocean surface currents," *Nature*, vol.328, pp. 707-709, 1987.
- [8] C. W. Chen, "Performance assessment of along-track interferometry for detecting ground moving targets," *Proc. 2004 IEEE Radar Conf.*, Philadelphia, PA, April 26-29, 2004.
- [9] Yuhong Zhang, Abdelhak Hajjari, Kyungjung Kim, and Braham Himed, "A dual-threshold ATI-SAR Approach for detecting slow moving targets," *Proc. IEEE International Radar Conference (Radar05)*, Arlington, VA, May 9-12, 2005.
- [10] D. A. Imel, "AIRSAR along-track interferometry data," *AIRSAR Earth Science and Applications Workshop*, March 4-6 2002.

- [11] E. Chapin, "User guide for processing AIRSAR data using the IFPROC and JurassicProk Processors Draft Version 0.5," *Technical memorandum*, Jet Propulsion Laboratory, February 20, 2004.
- [12] M. Soumekh, *Synthetic Aperture Radar Signal Processing with MATLAB algorithms*, Wiley, New York, 1999.
- [13] D. R. Wehner, *High-Resolution Radar*, 2nd Ed., Artech House, Inc., Norwood, MA, 1995.
- [14] R. Bamler and P. Hartl, "Synthetic aperture radar interferometry," *Inverse Problems*, vol. 14, R1-R54, 1998.
- [15] R. Nitzberg, *Radar Signal Processing and Adaptive Systems*, Artech House, Inc., Norwood, MA, 1999.
- [16] M. Soumekh and B. Himed, "SAR-MTI Processing of Multi-Channel Airborne Radar Measurement (MCARM) Data," *Proc. IEEE Radar Conf.*, Long Beach, CA, May 2002.